Lukas Wiesinger, BSc

Application of Laser Interferometric Vibrometry for the determination of density fluctuations in a swirl stabilized methane flame

MASTERS THESIS

in fulfillment of the requirements for the academic degree
Diplom-Ingenieur

submitted to

Graz University of Technology

First Reviewer and Supervisor

Ao.Univ.-Prof. Dipl.-Ing. Dr.techn. Jakob Woisetschläger
Institute of Thermal Turbomachinery and Machine Dynamics,
Graz University of Technology

Co-Supervisor

Dipl.-Ing. Felix Greiffenhagen
Institute of Thermal Turbomachinery and Machine Dynamics,
Graz University of Technology

This thesis was funded by the Austrian Science Fund FWF, project I2544-N30

Graz, October 2017

"I was born not knowing and have had only a little time to change that here and there."

Richard P. Feynman

Contents

Eidesstattliche Erklärung
Declaration of Authorship

Ich erkläre an Eides statt, dass ich die vorliegende Arbeit selbstständig verfasst, andere als die angegebenen Quellen/Hilfsmittel nicht benutzt, und die den benutzten Quellen wörtlich und inhaltlich entnommenen Stellen als solche kenntlich gemacht habe. Das in TUGRAZonline hochgeladene Textdokument ist mit der vorliegenden Diplomarbeit identisch.

I declare that I have authored this thesis independently, that I have not used other than the declared sources/resources, and that I have explicitly indicated all material which has been quoted either literally or by content from the sources used. The text document uploaded to TUGRAZonline is identical to the present master thesis.

Graz, October 31, 2017 Lukas Wiesinger

Acknowledgment

The present thesis was written at the Institute of Thermal Turbomachinery and Machine Dynamics at Graz University of Technology and was funded by the Austrian Science Fund FWF, project I2544-N30.

For all the support, regarding experiments and theory, I would like to thank my supervisors Ao.Univ.-Prof. Dipl.-Ing. Dr.techn. Jakob Woisetschläger and Dipl.-Ing. Felix Greiffenhagen.

The author thanks Dipl.-Ing. Dr.techn. Andreas Marn for sharing his insight and expertise in acoustics. Additionally I would like to thank Ao.Univ.-Prof. Dipl.-Ing. Dr.techn. Gerhard Graber for valuable hints and equipment used during the experiments.

Furthermore I would like to thank my parents Johann and Magdalena Wiesinger for supporting me all those years.

Abstract

To achieve nowadays emission goals for turbines, engineers are faced with a difficult challenge. Thus combustion processes - lean in pollutant but with higher thermal instabilities - have been developed. These thermal instabilities tend to shift the ideal point of operation, lead to additional thermo-acoustic emissions and harm the combustor and its surrounding. In the flame, the fluctuations in density can be directly related to the heat release fluctuations.

The improvement on Laser Interferometric Vibrometer during the last years - a technology normally used for the detection of surface vibrations - proofed to be sensitive and accurate enough to determine density fluctuations and thus heat release fluctuations in the flame. Now a measurement technique is available, which allows to resolve the density fluctuations and therefore the heat release fluctuations locally. With this novel tool a fast determination during the development process of turbine burners is possible.

The first part of this thesis focuses on investigations regarding filter functions (windowing) for discrete Fast Fourier Transforms and how they are used in the evaluation routines to obtain quantitative and reliable results.

In the experimental part, the aim was to proof that the Laser Interferometric Vibrometer is even capable to detect acoustic emissions emitted by the flame. Additionally an experiment, first performed by J. Peterleither, was repeated and the results were confirmed.

Kurzfassung

Um die heutzutage festgelegten Emissionsziele für Turbinen einzuhalten, werden Ingenieure mit einer schwierigen Herausforderung konfrontiert. Es wurden Verbrennungsprozesse entwickelt, die schadstoffarm, jedoch mit höheren thermischen Instabilitäten behaftet sind. Diese thermischen Instabilitäten beeinflussen den idealen Betriebspunt, führen zu zusätzlichen thermoakustischen Emissionen und regen Brennkammer und Anbauteile zum Schwingen an. In der Flamme können Schwankungen in der Dichte direkt mit Wärmefreisetzungsfluktuationen in Zusammenhang gebracht werden.

Die Verbesserung der Laserinterferometrischen Vibrometer in den letzten Jahren, ursprünglich zur Diagnostik von Oberflächenvibrationen verwendet, hat sich als sensitiv und genau genug erwiesen, um Dichteschwankungen und Wärmefreisetzungsschwankungen in Flamme zu bestimmen. Diese Messtechnik erlaubt es, Dichteschwankungen und damit die Wärmefreisetzungsschwankungen lokal aufgelöst zu bestimmen. Somit ist ein neuartiges Messverfahren zur schnellen Bestimmung der Dichteschwankungen in der Flamme während des Entwicklungsprozesses von Brennern gegeben.

Der erste Teil dieser Arbeit konzentrierte sich auf Filterfunktionen (Windowing) für die diskrete Fast-Fourier-Transformation, wie Sie in den Auswerteroutinen verwendet werden um quantitative und verlässliche Werte zu erhalten.

Im experimentellen Teil konnte gezeigt werden, dass Laserinterferometrische Vibrometer sogar in der Lage sind, die Schallemissionen der Flamme zu erfassen. Zusätzlich wurde ein Experiment wiederholt und bestätigt, welches zuvor von J. Peterleither durchgeführt wurde.

List of Figures

List of Tables

Nomenclature

A	$-$	Amplitude
a	$-$	generic constant
b	$-$	generic constant
c	m/s	speed of sound
c_{spec}	$-$	mole fraction
d_c	m	critical distance
$ENBW$	$-$	equivalent noise band width
f	Hz	frequency
f_{res}	Hz	frequency resolution
FTF	$-$	flame transfer function
G	$-$	Gladstone-Dale constant
I_r	W/m^2	sound intensity
k_{vib}	m/V	LIV calibration factor
L	m	geometrical length
$\dot{m}$	kg/s	mass flow
n	$-$	refractive index
n	$-$	positive integer variable
N	$-$	sample points
OPL	m	optical path length
p	Pa	pressure
P_{far}	W	sound power in the far field
P_{th}	W	power of burner
$\dot{Q}$	W	total heat release rate
q_v	W/m^3	volumetric heat release
r	m	radial distance
RT_{60}	s	reverberation time
s	m	path length
s	J/kgK	volumetric entropy
SL	S	Sample Length
SR	S/s	Sample Rate
t	s	time
U	V	Voltage
V	m^3	Volume
v	m/s^{-1}	velocity
v_r	m/s^{-1}	sound particle velocity
x, y, z	$-$	Cartesian coordinates

α	$-$	acoustic absorption coefficient
$\Delta\theta$	rad	phase difference
κ	$-$	heat capacity ratio
λ	m	wavelength
ν	m	wavelength of the laser light
ϕ	$-$	equivalence ratio
φ	rad	phase, for FFT
θ	rad	phase shift, for FFT
ω	Hz	frequency of the laser light

List of Abbreviations

AC	alternating current or alternating component
A/D	Analog/Digital
CFT	Continous Fourier Transform
cps	cycles-per-second
CPSD	Cross Power Spectral Density
DC	Direct Contribution
DFT	Discrete Fourier Transform
DSP	Digital Signal Processing
ENBW	Equivalent Noise Band Width
FA	Fourier Analysis
FFT	Fast Fourier Transform
FS	Fourier Synthesis
FTF	Flame Transfer Function
ICAO	International Civial Aviation Organization
Im	Imaginary part
LIV	Laser Interferometric Vibrometer
LPM	Lean Premixed combustion
NENBW	Normalized Equivalent Noise Bandwith
OEM	Original Equipment Manufacturer
OPL	Optical Path Length
PIV	Particle Image Velocimetry
PM	Photomultiplier
PP-probes	Pressure-Pressure probes
PPM	Perfectly Premixed
PSD	Power Spectral Density
PS	Power Spectrum
RMS	Root-Mean-Square
Re	Real part
sinc	sinus cardinalis
SL	Sample Length
SNR	Signal to Noise Ratio
SR	Sample Rate
TPM	Technically Premixed
VDI	Verband Deutscher Ingenieure
WT	Wavelet-Transformation

1 Introduction

1.1 Motivation

The development and welfare in today's society depends greatly on the easy access and availability of energy. Since the industrial revolution, gas turbines have been a major contributor to electrical energy. Therefore energy depletion and its environmental effects have become a controversial issue of society. Thus, gas turbine manufacturers are strained to develop more energy efficient systems and to reduce emissions.

Engineers have been working the last decades to improve the efficiency of combustion in gas turbines. The challenge to increase efficiency and reduce pollutant concentrations is challenging, due to conflicting goals. Higher combustion temperature lead to thermal NO_X production but yields towards higher efficiencies. Rich combustion will increment the amount of CO and soot produced. Lean combustion is prone to thermal instabilities which lead to higher combustion noise, a serious topic in aero-engines. [1]

To solve this problem gas turbine designers developed various combustion methods, using pre-treatment or/and post-treatment techniques to ensure lower pollutant emissions. The standard technique used by many ***original equipment manufacturers (OEM)*** nowadays is ***Lean Premixed Combustion (LPM)***. [1]

With LPM it was possible to reduce NO_X emissions and increase efficiency. As a disadvantage heat release fluctuations due to lean fuel mixture lead to thermo-acoustic oscillations. These oscillatory instability are the result to incomplete combustion and unsteady, highly turbulent flow conditions and have hindered the development of LPM burners in the last decades. The oscillations caused by these combustion instabilities can reach high amplitudes, severe enough to damage turbomachinery parts. In worst-case scenario thermo-acoustic oscillations will lead to cracking or destruction of burner and impeller, as seen in figure 1.1 [2].

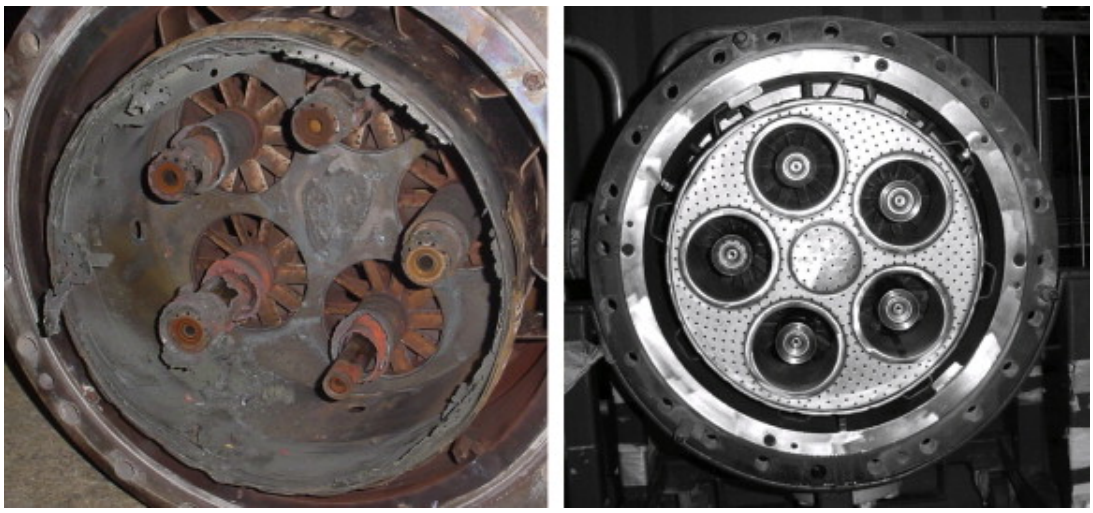

Figure 1.1: Example for damage by thermo-acoustic oscillations [2]

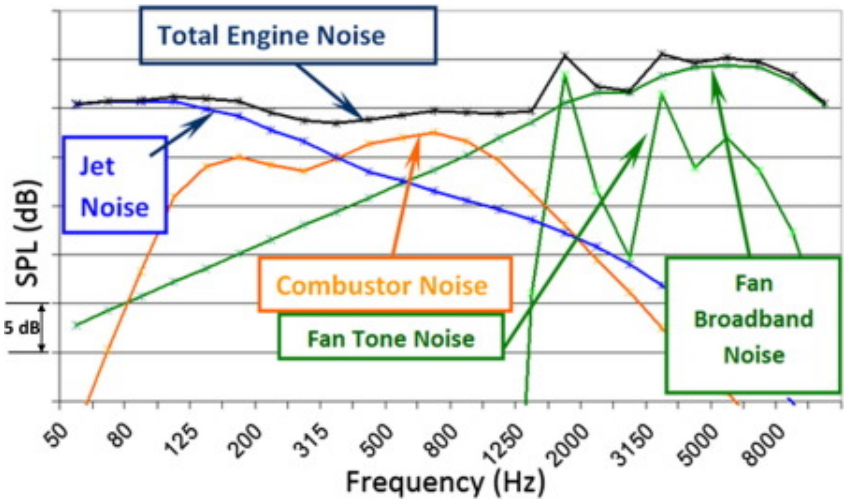

Figure 1.2: Noise sources from air planes [3]

On the one side LPM increases gas turbine efficiency and reduce the pollutant emissions, on the other side thermo acoustic oscillations lead to additional acoustic emissions. These concerns effects especially aviation. The International Civil Aviation Organization (ICAO) set standards for noise reduction from air planes. The newest regulation, CHAPTER 14, reduces the noise another 6dB from CHAPTER 4 [4]. Noise emission from the engine, the jet and the fans have already been reduced considerably, thus combustion becomes a more considerable source of noise as seen in figure 1.2. [3] .

Thus information about the heat release fluctuations are sought after by the turbine developer, to determine a stable point of operation and reduce thermo-acoustic oscillations. A commonly chosen parameter for modelling and prediction is the ***Flame Transfer Function (FTF)***.

The determination of the FTF is accomplished by the determination of total heat release fluctuations in the flame $\dot{Q}'$ and the inlet velocity oscillations v'. With the mean overall heat release $\bar{Q}$ can be calculated from the mass flow and the mean velocity $\bar{v}$ as well. Equation 1.1.1 shows the discussed relation.

$$\frac{\dot{Q'(f)}}{\bar{\dot{Q}}} = \frac{v'(f)}{\bar{v}} * FTF(f) \tag{1.1.1}$$

Following methods are used nowadays to determine the variables of the FTF:

- Chemiluminescence from OH^* to determine $\dot{Q}$ and thus $\dot{Q}'$
- Constant Temperature Anemometry (CTA) for the v and thus v'
- Laser Doppler Anemometry (LDA) for v and thus v'
- Calculation of $\dot{Q}$ and $\bar{v}$ via the mass flow rates

In former projects of TU Graz (J. Woisetschläger) it was shown that ***Laser Interferometric Vibrometers (LIV)*** are suitable interferometric instruments to determine the heat release fulctuations $\dot{Q}'$ and $\dot{q}'$ (locally resolved heat release fluctuations). Besides $\dot{Q}'$, $\bar{v}$ and v' can be measured with a second LIV

or with a camera based LIV-system, which is topic of a research cooperation between TU Dresden (J. Czarske, A. Fischer) and TU Graz (J. Woisetschläger, F. Greiffenhagen). Such a full-field LIV records field information with all spatial and temporal correlations. This is the task of FWF funded project I2544-N30.

Thus, LIV represents an interesting alternative to chemiluminescence and LIV enhanced with a high speed camera array is capable to capture the FTF in a single measurement procedure. This will reduce measurement and development time of combustors.

1.2 Objective

The objective of this thesis was to verify the capability of LIV to determine heat release fluctuations and sound emission from a flame quantitatively. To tackle this objective it was necessary to optimize the data evaluation routines and to discuss possible error sources.

During the optimzation of the Fast Fourier routines a thorough anaylsis of uncertainties and a literature study was performed in this thesis, concerning the use of filter functions and their impact on the results. A discussion how windowing and sampling will influence the results is given in section 2.2.2 with the routines presented in Appendices A.3 A.4 A.5.

These Matlab routines were then applied to quantitatively record the acoustic field emitted by the flame. The global recordings are already discussed by [5] [6] [7]. The quantitative local information recorded in this thesis is important since Strahle [8] assumed a single oscillating monopole with a uniform sound field. But a local disturbance under 45° in flow direction was found [9]. Assuming an influence of the temperature field and the flow field on the shape of the sound emission has to be verified by quantitative recordings of the near field. Such a near field recording will be possible with the data received from the LIV measurements performed in this thesis. To accomplish this objective and verify the results a gradual approach with a sound speaker as sound source as first approximation was chosen.

One objective of this thesis was to showcase the capability of LIV to determine quantitatively acoustic fields, as it was shown before by [7] [5] [6]. Since Strahle [8] assumed a single oscillating monopole the shape of the flame should be determined to verify his theory. This was possible with the data received from an LIV measurement.

Additionally, another LIV measurement of the flame was performed by the author, in order to obtain the local density fluctuations $\dot{\rho}'$ in the field and relate this information with the sound-power recorded with a microphone array. Note that $\dot{\rho}'$ can be related to $\dot{Q}'$(see section 2.1). The theory and relations to this measurements were given by Strahle [8] and Peterleithner et al. [10] and can be found in section 2.1 (additional information on the development of the relation between density and heat release, as found in literature, is provided in the Appendix) This measurement of local density fluctuations was used to verify results from former research with previous FFT routines.

1.3 Literature

This section presents relevant books and papers used during this thesis which present and discuss the problem or enhance the readers capability for a better understanding and approach to the problem. Additionally a recap of the work on the institute can be found at the end.

Problems with heat release fluctuations have been observed since a long period of times. One of the first remarkable incidents were the pogo oscillation (from the pogo stick) of the Saturn V rocket, used for the moon mission in the 1960s and the 1970s. The combustion oscillation during start and in flight caused severe problems. During the second stage burn, the engine experienced a vibration amplitude of $333ms^{-2}$ at 16 Hz, which lead the thrust frame to oscillate 6.6 cm peak to peak amplitude and resulted in an emergency shut down of the second stage. [11]

Strahle (1972) was one of the main contributors relating density fluctuations in the flame to the sound power emitted by combustion [8]. Thus thermo-acoustic oscillations can be referred to the density fluctuation in the flame caused by combustion instabilities.

Years later, 1995, Keller published a paper which outlines thermo-acoustic oscillations in gas turbine combustors with premixed fuel. [12].

In 1997 the "Verein Deutscher Ingenieure" (VDI) published a paper in which combustion oscillations in a $170MW$ gas turbine combustor had been observed. The problem was solved by anti-cyclical high speed fuel injection. [13]

In more recent years-thermo acoustic oscillations have been simulated for the F1 rocket engine, which was used in the Saturn V rocket. This resulted in the conclusion that the injector design has major impact on those oscillations. [14]

Further contributors followed: Stow in 2001 [15], Lieuwen in 2002 [16].

For a detailed insight in combustion and transport equations in a reactive gas Williams book "Combustion Theory" (2000) [17] can be referred to.

Questions regarding interferometry or optics are answered in Hecht's text book "Optics" [18], which is an experimental and fundamental text book throughout the world.

Former experiments, similar to those made in this thesis, but on non-reacting flows have been performed by Zipser et. al (2002) [7], Gren et al. (2006) [5] or Harlan et al. (2007) [6].

When performing ***Fast Fourier Transforms (FFT)*** on the received data the reader is referred to Lyons [19]. For more advanced topics Oppenheim et al. [20] can be consulted. An excellent web resource is "The scientist and Enginner's Guide to Digital Signal Processing" by Smith [21].

Concerning filters for FFT, also called windowing, one of the most profound papers was published by Harris (1978) [22]. Further information can also be found in [19], [21]. A mentionable tutorial on filters and their impact on the amplitude was published by Scholl [23].

First investigations at the Institute of Thermal Turbomachinery and Machine Dynamics (TTM) at the Technical University Graz were carried out by Mayrhofer et al. (2000) [24]. The authors were able to detect density fluctuations caused by vortex shedding in the wake of a turbine blade. Further investigations followed by Mayrhofer et al.(2001) [25] and Hampel et al.(2006) [26] to record local fluctuations of the flow field. Giuliani et al. (2006)[27] and Köberl et al. (2010) [28] investigated reactive flows with LIV the first time. Further contributions were made by Leitgeb et al. (2013) [29], where a comparison between LIV and ***Photomultiplier (PM)*** measurement was performed. The second part of the project is focused on prediction of combustion noise by the means of LIV measurements. Thus the burner in the acoustic measurement lab was redesigned and validate by Leitgeb [30] and Giuliani et al. [31]. Peterleithner et al. (2015) [32] characterized the burner via ***particle image velocimetry (PIV)*** , LIV and chemiluminescence. Later on Peterleithner et al. (2016) [33] compared the FTF obtained via LIV

measurements and PM measurements. During latest research from Greiffenhagen et al. (2017) [34] it was possible to predict the sound power emitted from the flame via LIV and compare it to the microphone array. Further research aims to the development of an industrial measurement system in cooperation with the Technical University of Dresden.

2 Materials and Methods

2.1 Interferometry

This section presents the relation between heat, pressure and its influence on the interference of the measured signal.

Laser Interferometric Vibrometers (LIV) can detect the changes in ***Optical Path Length (OPL)*** between a reference beam and the object beam and therefore provide line of sight data.

The OPL is defined as followed:

$$OPL = \int_l n(s,t)\ ds \tag{2.1.1}$$

In the case of the chosen experiment, it will result in a dependency in a single direction, z as followed:

$$OPL = \int_l n(x,y,z,t)\ dz \tag{2.1.2}$$

Which can be understood as the path integral along the trace of the ray.

Where the ***refractive index n*** is depended on density and medium. L describes the geometrical length to the measurement object or the mirror. Therefore n changes its value in the directions x,y,z.

Deriving equation 2.1.3 in time results in:

$$\frac{\partial OPL}{\partial t} = L\ \frac{\partial n(x,y,z,t)}{\partial t} + \frac{\partial L}{\partial t}\ n(x,y,z,t) \tag{2.1.3}$$

Since in the experiment the distance to the mirror or the retroreflector is fixed, $\dot{L}$ can be discarded. This results in:

$$\frac{\partial OPL}{\partial t} = L\ \frac{\partial n(x,y,z,t)}{\partial t} \tag{2.1.4}$$

Thus the OPL difference ΔOPL is related to a phase difference $\Delta\theta$ between the reference beam and the object beam by its wavelength λ (633 nm for a Helium-neon laser) and its corresponding phase 2π. Since the object beam has to pass the experiment twice, the result is factored by 2 and as the out-of plane movement of the signal is counted as positive, the voltage term is negative. These relations can be seen in equation 2.1.5

$$\frac{\partial(\Delta\theta(t))}{\partial t} = \frac{4\pi}{\lambda}\frac{\partial(\Delta OPL(t))}{\partial t} = \frac{4\pi}{\lambda}\int_l \frac{\partial(\Delta n(x,y,z,t))}{\partial t}\ dz = \frac{4\pi}{\lambda}\ k_{vib}\ U(t) \tag{2.1.5}$$

The output ***voltage U(t)*** of the LIV is scaled by the factor $\boldsymbol{k_{vib}}$ which will then result in changes of the OPL.

The ***Gladstone-Dale constant*** $\boldsymbol{G(\nu, c_{spec.})}$ relates n with ***density*** ρ as in equation 2.1.6. With ν being the frequency of the laser light.

$$n(x, y, z, t) - 1 = \rho(x, y, z, t)\ G(\nu, c_{spec.}) \tag{2.1.6}$$

Since $G(\nu, c_{spec.})$ does not dependend on temperature or pressure, but on the mole-fractions $c_{spec.}$ in the flame locally, corrected data in the flame was provided from previous research by Greiffenhagen, Peterleithner and Woisetschläger. [34].

Looking at equation 2.1.6 and equation 2.1.4, a change in density can be directly related to a change in the OPL.

Since in the experiment ideal gas was assumed, with Gibbs phase rule the degree of freedom is 2. Hence $\boldsymbol{\rho}$ can be described as function of the ***pressure p*** and the ***entropy s***. The total differential can be written as followed:

$$d\rho(s, p) = \frac{\partial \rho(s, p)}{\partial p}\Big|_s dp + \frac{\partial \rho(s, p)}{\partial s}\Big|_p ds \tag{2.1.7}$$

In equation 2.1.7 the first term represents the change in p at constant entropy, the second term represents the change in entropy with constant pressure, which will later on be transposed to the reversible heat.

The derivation of equation 2.1.8 can be found in the Appendix A.1.

Where the instantaneous value of the ρ can be expressed through the averaged $\bar{\rho}$ value and the fluctuation value ρ'. Hence A.1.8 will result in 2.1.8, assuming small convection of density gradients (small Mach numbers):

$$\frac{d\rho(s, p)'}{dt} = \frac{1}{c^2}\frac{dp'}{dt} - \frac{\kappa - 1}{c^2}\frac{dq_v'}{dt} \tag{2.1.8}$$

With $\boldsymbol{q_v}$ the ***volumetric heat release*** $[W/m^3]$.

Within the flame a more detailed transport equation has to be used, Williams's equation, which can be found in the appendix A.2.

Relating equation 2.1.4 with equation A.1.7 and 2.1.6 results in the $\frac{\partial OPL}{\partial t}$ which can be directly correlated to the the analogue voltage $U(t)$ signal from the LV.

$$\frac{\partial OPL}{\partial t} = L\frac{\partial n}{\partial t} = \frac{\partial \rho}{\partial t}G(\nu, c_{spec.})L = G(\nu, c_{spec.})L\ \{\frac{1}{c^2}\frac{dp}{dt} - \frac{\kappa - 1}{c^2}\frac{dq_v}{dt}\} \tag{2.1.9}$$

When performing the experiment far away from the flame or on a speaker, it can be assumed, that q_v has no influence and therefore the second term of the equation can be neglected.

This will result in equation 2.1.10 ,

$$\frac{\partial OPL'}{\partial t} = G(\omega)L\ \frac{1}{c^2}\frac{dp'}{dt} \tag{2.1.10}$$

Looking at equation 2.1.3 we see that:

$$U'(t)\ \propto\ \frac{\partial p'(t)}{\partial t} \tag{2.1.11}$$

which is used to pose the results of the acoustic emission measurment via LIV. See section 3.2.

For the relation between density fluctuations in the flame and the density fluctuations in the acoustic far field we know from Strahle [8]

$$\rho'(r,t) = \frac{1}{4\pi c_0^2 r}\frac{\partial^2}{\partial t^2}\int_{V_{fl}} \rho'(r_0, t - \frac{r}{c_0})dV(r_0) \tag{2.1.12}$$

with ρ_T representing the density fluctuation in the flame, r the distance of the observer and c_0 the local speed of sound under ambient conditions.

Whereas ρ', the density fluctuations in the far field, can be related to the ***sound power*** (P_{far}) in the far field as followed

$$P_{far} = \frac{1}{4\pi c_0^2 r}\frac{\partial^2}{\partial t^2}\Big(\int_{V_{Fl}} \rho'_T(r_0,t) - \frac{r}{c_0}dV(r_0)\Big)^2 \tag{2.1.13}$$

Therefore the sound power P_{far} can be directly related to the second time derivative of the density fluctuations, seen in equation 2.1.14.

$$P_{far} \propto -\int_V \frac{\partial^2 \rho'}{\partial t^2} \tag{2.1.14}$$

Hence a measurement of sound power provides a comparative method to the measurement of the ρ' within flame with LIV.

For a detailed insight see: [8] [34].

2.2 Fourier Analysis

This section presents the ***Fourier Analysis (FA)*** and deepens the most important properties - for this master thesis in mechanical engineering - in the following chapters. The Fourier analysis is the decomposition of a function in its harmonics by a Fourier transform, while the rebuilding of the function by an inverse Fourier transform is called ***Fourier Synthesis (FS)***.

The ***Fourier transform (FT)***, or ***Fast Fourier Transform (FFT)*** is discussed in numerous articles and text books. In 2000 it was ranked by the the magazine "Computing in Science and Engineering" as one of the top ten computer algorithms "... with the greatest influence on the development and practice of science and engineering in the 20th century." [35] The authors stated: "The FFT is perhaps the most ubiquitous algorithm in use today to analyze and manipulate digital or discrete data" [35]

An overview of different applications of the Fourier Transform can be found in chapter 1 of the text book "The Fast Fourier Transform and its Applications" from E. Oran Brigham [36]. The author lists more than 70 examples in which the FFT can be used.

In the year 1822 Jean-Baptiste Joseph Fourier(1768-1830) published a script,"Théorie analytique de la chaleur" (Analytical Theory of Heat) [37] , in which he examines the thermal conduction in materials. Fourier stated that any periodic signal or function can be decomposed in a sum of harmonic functions, possibly an infinite sum. Thus, each periodic function can be represented by a linear combination of sine and cosine functions. Fourier used this theorem to solve the well-known Fourier's-law which describes the thermal conduction in a solid body. [38]

Equation 2.2.1 shows the Fourier decomposition of a function into a series of harmonic functions. In 1829 Johann Peter Gustav Lejeune Dirichlet (1805-1859) stated the convergence of the Foruier series. In 1853 Georg Friedrich Bernhard Riemann (1826-1866) introduced a precise notion of function and integral, and introduced the Fourier coefficients. These coefficients, a and b, can be seen in equation 2.1.1. [38] [39]

$$x(t) = a_0 \ + \sum_{n=1}^{m=\infty} a_n cos(2\pi f n) \ + \sum_{n=1}^{m=\infty} b_n sin(2\pi f n) \ \ n = 1, 2, 3 \ldots \tag{2.2.1}$$

with $n \in \mathbb{N}$, $a0$ the ***directe contribution*** (DC), a_n and b_n the sine and cosine coefficients.

In 1966 Lennart Carleson (born 1928) and Richard Allen Hunt (1937-2009) were able to prove that the Fourier series of every steady function will converge. 1965 was an important year for engineering. James William Cooley (1926-2016) and John Wilder Tukey (1915-2000) developed an efficient algorithm with which it was possible to compute the Fourier coefficients of the Fourier series fast. This algorithm is known as the first ***Fast Fourier Transform (FFT)*** used to compute the ***Discrete Fourier Transform (DFT)***. For better understanding above FT is then often called ***Continous Fourier Transform (CFT)*** [40] [38].

After Cooley and Tukey presented the FFT algorithm, various improvements and further algorithms have been developed. At this point, it is worth to mention that the Coole-Tukey algorithm is also known as a Radix-2-algorithm and requires the power of 2 in its sampling length (SL) for computing the FFT in programs using this algorithm.

A further enhancement was the ***Wavelet-Transformation (WT)*** in 1980, which is used for example in astrophysics for image processing or slightly modificated in the well know JPEG file format for pictures. In the end it took about 150 years to reach the current state of the Fourier transform. [38]

In the following sections FFT and DFT will be discussed, taking in consideration the needs of this thesis in the determination of frequency, phase and amplitude of a signal recorded in the time domain. Filtering via window-functions will be discussed theoretically and in experiment. Possible errors during measurement and signal processing are also treated.

For further reading on the basics of the FT: [39] [41] [36], for a better insight on ***digital signal processing***

(DSP): [19] [23] and for windowing the reader may refer to: [22]

2.2.1 Basics of the discrete Fourier transform

This chapter discusses the basic principles of the DFT insofar as they are relevant to this work.

Digital signal processing treats sampled functions of finite length with equally spaced samples. The rate of sampling is called ***Sample Rate (SR)*** and is given in samples per second $[S/s]$. In this thesis, the DFT converts these samples of the signal function from the time domain into a set of equally-spaced, complex-valued frequency samples in the frequency domain by a FFT algorithm named pwelch in Matlab. The DFT helps to determine the frequencies present in the signal, their amplitude or power and their phase relative to a reference signal (by correlation). The DFT is therefore the frequency domain representation of the sampled signal.

The Nyquist-Shannon Sampling Theorem (Harry Nyquist, 1889-1976, and Claude Elwood Shannon, 1916-2001) states that "If a function x(t) contains no frequencies higher than W cps, it is completely determined by giving its ordinates at a series of points spaced 1/2 W seconds apart." [42] With ***cycles-per-second (cps)*** or Hertz. From this theorem, we derive that when a signal is sampled with 1024S/s in the time domain, the maximum frequency in the frequency domain is 512Hz.

In the complex DFT, the FFT transforms a sample with N sample points to a spectrum with N frequency values. This number N is called the ***Sample Length (SL)*** and is given in samples [S]. Let us assume we have a sample with SL 1024S, sampled with a SR of 1024S/s. This SL then corresponds to a duration of 1 second. The smallest period represented by this sample is 1Hz, thus the frequency resolution between sample points in the frequency domain is 1Hz. Assuming a SL equal 2048 S, the time duration of this sample is 2 seconds, representing a smallest period of 1/2Hz, resulting in a 1/2Hz frequency resolution in the frequency spectrum.

When the time signal contains frequencies above the Nyquist frequency these high frequencies will be under sampled and will be represented by its components lower than the Nyquist frequency. In above example 513Hz will be aliased as 511Hz, 514Hz as 510Hz. This is called (frequency domain) aliasing. (The signals masquerades as other, alias another one). Whenever higher frequency contributions cannot be avoided, a low-pass filtering must be applied to the input signal first. Effects of aliasing can be seen in figure **??**. The rotor blades are pictured wrong, due to too low sampling rate of the camera.

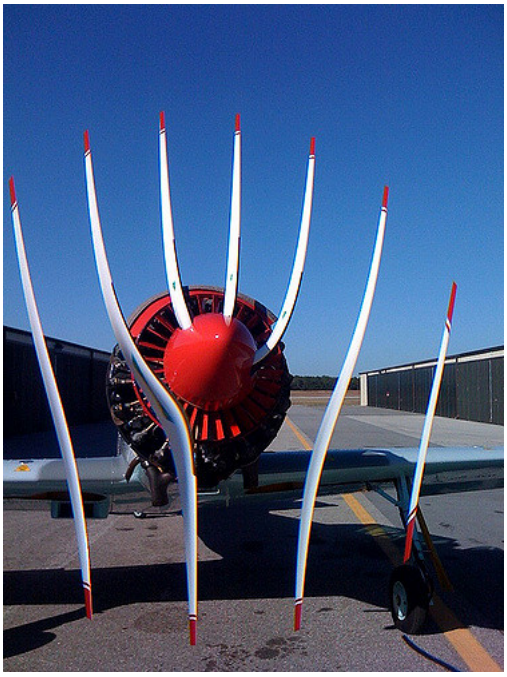

Figure 2.1: Example for aliasing on a rotor blade with too low shutter speed of the camera [43]

Due to the periodic nature of the DFT each sample in the time domain is viewed as periodic result in an infinite signal for FT. If the periodic samples contain a strong step function at its joints, the frequency contributions from this step function will result in new frequency components not inherent to the signal, called spectral leakage. This effect cannot be avoided when a sample of finite length is used, but can be minimized by a window function multiplied onto the sample, helping the sample to reach the same values at the joints. For windowing see 2.2.2.

Whenever a FFT is applied, the sample might be extended to 2^n sample points by zero padding for FFT algorithms that require that. According to the convolution theorem each multiplication of two functions in the time domain results in a convolution of the two frequency spectra in the frequency domain. Zero padding can be used to enhance the frequency resolution, alleviate the effect of scalloping loss (see [19], Chapter 3.10) but does not improve that data set physically. Thus, zero padding will alter the frequency spectrum and should be avoided.

The FFT is one method to calculate the DFT and uses complex numbers to describe the single points in the time and frequency domain (real and imaginary part). While the real DFT uses ***N sample points (=SL)*** from the time domain to create N/2 +1 frequency points in the frequency domain, the complex DFT uses two N point samples in the time domain (real and complex) to create 2 N point samples in the frequency domain. These two samples in the frequency domain hold the cosine (real part) and sine (imaginary part) waves, while the real part of the time domain sample contains the data, and the imaginary part of the time domain sample is set to zero. After performing the FFT by decomposing the signal in 2N steps, performing the FT and synthesizing the spectra, sample points 0 through N/2 (real and imaginary part) in the frequency domain correspond to the DFT spectrum. The complex DFT produces a two-sided spectrum with the real part from point N/2+1 equals the real part from N/2-1, and the the complex part of N/2+1 equals the negative complex part of N/2-1. Only point 0 and N/2 have no matching partners.

Figure 2.2 shows the time domain and the discrete frequency domain of a signal. Note that the DFT amplitude has to be scaled with the factor $1/f_{max}$ to exceed in a correct value, when calculated with the Matlab fft() command. From Fourier synthesis the time domain signal is given by equation 2.2.2.

$$f(t) = 20 + 1.5\ sin(10\pi t) + 0.0625 sin\ (40\pi t + \pi/2) \tag{2.2.2}$$

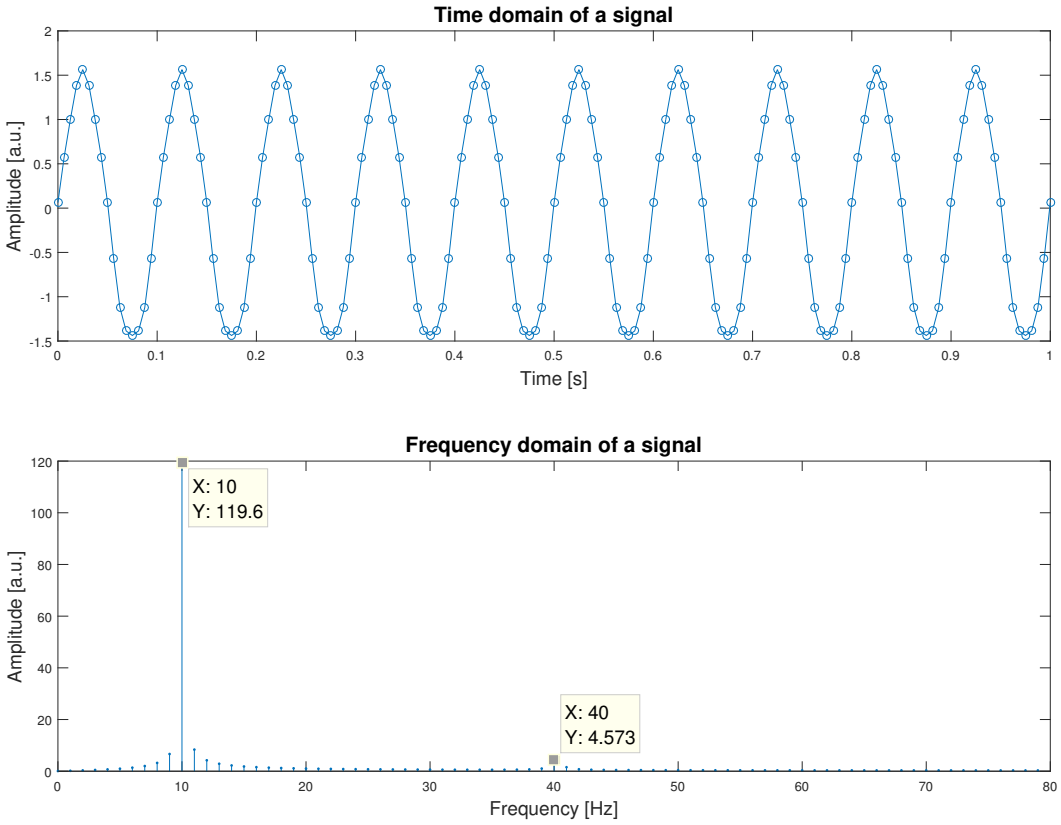

Figure 2.2: Example for a DFT calculated with the Matlab fft() command

Since the first half of the complex frequency spectrum from the DFT contains all the important information for signal analysis, the second half can be discarded. [23]

The pwelch command from Matlab "returns the ***power spectral density (PSD)*** estimate, pxx, of the input signal, x, found using Welch's overlapped segment averaging estimator" [44]. Multiplying the power spectral density by the equivalent noise band with (see section 2.2.2) results in the ***Power Spectrum PS***), providing the frequency-related power of a signal at a given frequency (or the average within a given frequency bin).

The sum (integral) of the single frequency values (except 0) in the power spectral density equals the square of the standard deviation in the time domain sample ***(Parseval's theorem)***. See equation 2.2.3.

Such a summation of the power spectrum results in the total power contained in the signals fluctuations and can be interpreted as the conservation of energy in a signal.

$$\sum_{m=1}^{M} PS(f) = \frac{1}{N} \sum_{n=0}^{N} x_n(t)^2 \tag{2.2.3}$$

From equation 2.2.1 it is seen that frequency bin 0 contains the ***direct current or direct component (DC)*** contribution, while all other frequency bins contain the ***alternating current or alternating component (AC)*** parts of the signal up to the Nyquist frequency. The first bin, bin 0, represents the DC contribution. These DC values may have come from the DC contribution in the analog signal converted to a digital signal, or from imperfections introduced by the analog/digital (A/D) converter. Another source may also be truncation of discrete time signals when the analog input signal has an amplitude too high for the converter. DC components are important for the normalization of the $OH*$ radiation recorded by the ***PM*** and for audio files. For this work they are of no further interest. [19]

The single values in the discrete PS corresponds to the areas of the bins in a continuous spectrum (power per bin). The width of the bins f_{res} is given by the relation 2.2.4.

$$f_{res} = \frac{SR}{SL} = \frac{SR}{N} \tag{2.2.4}$$

If we have a $16kS/s$ SR and hand it over to our DFT in samples of 16kS SL a frequency resolution of 1Hz will be the result. Choosing SR=SL is very convenient since this will result in frequency data that needs no further manipulation when switching from a discrete to a continuous spectrum and will provide the power per unit (Hz).

This does not mean that this can be used in the following aspect: Choosing the frequency resolution on a "rougher" value, will widen the frequency bins and cover therefore more frequencies. A lower frequency resolution means that only the discrete frequencies of 0 Hz, 5Hz, 10 Hz and so on will be represented in the frequency spectrum. Frequencies that fall in between two bins will result in an amplitude in both bins (see sepctral leakage). To retrieve amplitudes from frequencies that tend to shift a bit in the experiment, windowing can be a solution. Therefore see section 2.2.2.

The root of the PSD provides the RMS amplitude. To obtain the ***amplitude spectrum AS*** from a power spectrum the RMS amplitude must be multiplied by $\sqrt{2}$. Figure 2.3 gives an overview on the calculation steps, from the time domain signal to the PS.

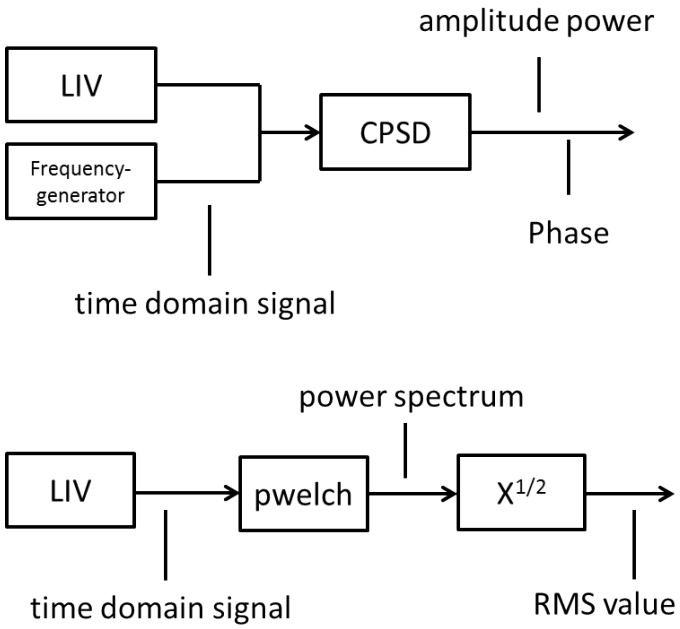

Figure 2.3: Schematic of calculation of DFT values

The resulting amplitudes do not exactly match the real values from equation 2.2.2. For obtaining exact amplitude values from a FFT various error effects have to be considered, which are explained in [23].

The values from the frequency bins are complex numbers and each frequency can be represented in a phasor diagram as it can be seen in figure 2.4. The ***real part (Re)*** is defined as the cosine part of the phasor and the ***imaginary part (Im)*** is represented through the sine. The angle between Re and the vector is defined as the phase φ, whereas φ is defined as: $\varphi = f * 2\pi * t + \theta$. A phase shift θ in frequency domain represents a time shift in time domain. So the corresponding signal lags or leads. This expression can also be written as in equation 2.2.5.

$$e^{i\varphi} = cos(\varphi) + i\sin(\varphi) \tag{2.2.5}$$

For an exact phase measurement a cross-correlation is used, which compares two signals by multiplication of spectra in the frequency domain, where the highest resulting value represents the frequency with the highest degree of correlation between two signals. With this information a ***cross power spectral density (CPSD)*** can be calculated. It is worth noting:

- The CPSD is the FT of the cross-correlation of two signals.
- The PSD is the FT of the auto-correlation of one signal.

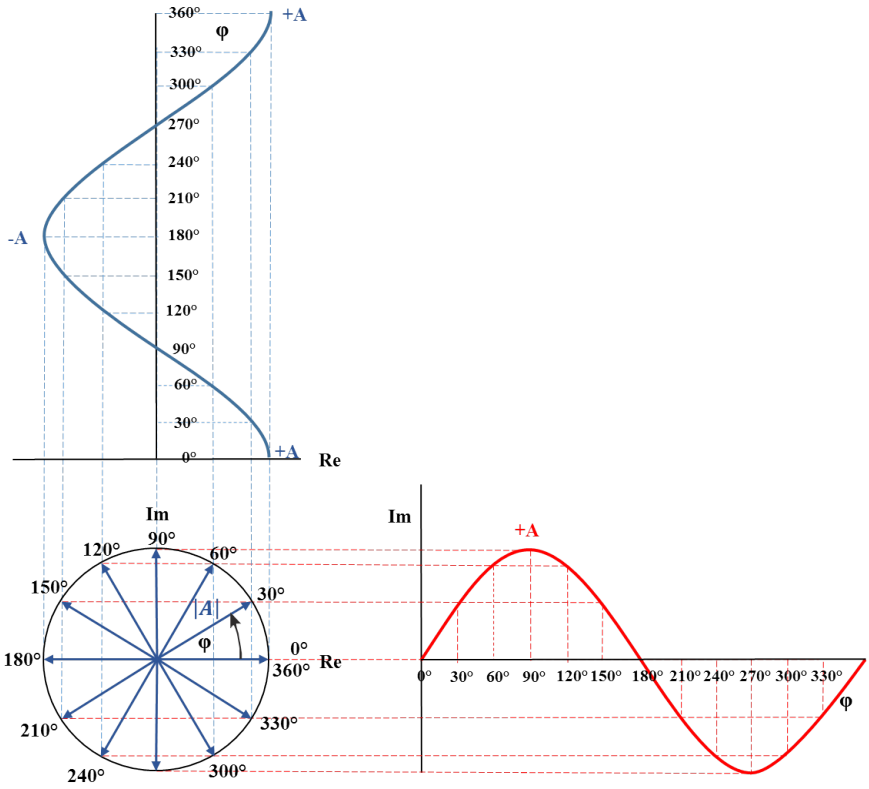

Figure 2.4: Example for phasor diagrams.

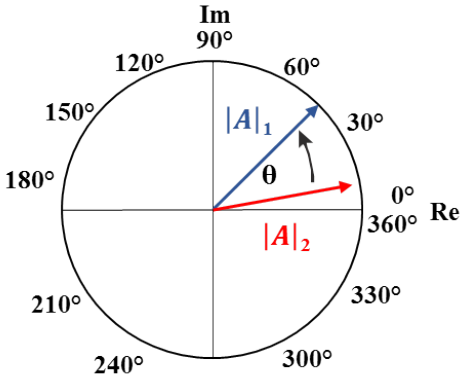

Figure 2.5: Example for phase shift between two signals

In Matlab the command cpsd() was used for calculation of correlation.

To obtain the phase shift θ between A_2 and A_1, from the CPSD as it can be seen in figure 2.5, the $atan(imag(X(f))/(real(X(f))$ is used. Where $X(f)$ represents the result of the according FFT frequency bin. In Matlab the commands atan2() or angle() can be used to obtain the modulo 2π phase shift between two signals.

To retrieve amplitudes and frequency from the flame or the speaker a FFT of the voltage signal was performed provided by the analog output of the laser interferometric vibrometer (LIV) (line of sight data). The CPSD was calculated correlating the LIV with the siren (signal generator), or correlating the LIV with a second LIV which was focused on a fixed position. For the speaker setup (see 3.2), the method appeared to be more reliable. The SR was 16384 S/s (2^{14}) and the SL 16384 S, which resulted in a frequency resolution of 1Hz. Due to turbulence and reflections, the sample time was set to 60 seconds, which appeared to be a good compromise between measurement time and precision. With the data of 60 s signal, it is possible to average the amplitude for each frequency with 60 values. This is also important when recording the refractive index field of the flame, since combustion is highly turbulent and a high number of frequency spectra must be averaged to obtain a good ***signal to noise ratio (SNR)***, as well as, in phase.

2.2.2 Windowing

When sampling real-world signals, the frequency domain results can be misleading, since the DFT is constrained to work on a finite set of N input values. If we take a look at eq 2.2.4 we see that for an infinite resolution in the frequency domain, the sample length must be infinite, in order to represent all frequencies present in the time domain signal exactly - which is not possible.

In figure 2.6 the effects of leakage is discussed. The blue line represents a FFT with a very long set of data and therefore approximates a CFT. The orange line is multiplied by a function that shortens the data set to 10% of its original information and sets values outside the window to 0. This filter is called the rectangular or uniform window. The signal is represented through a delta peak in the frequency domain. Taking a look at the second FFT signal, we can see side peaks "rolling" of the main peak, which are caused by the sharp corners on the rectangular window. This effect is called ***spectral leakage***. Since a multiplication of two signals in time domain results in a convolution of their Fourier transform, the leakage effect can be seen as the result of the convolution of the rectangular windows sinc function with the delta function of a single frequency signal. For a more detailed insight on the effect of leakage and the circularity of the DFT see [21], chapter 10.

When performing a DFT, signals which are not multiples of f_{res} will show the effect of spectral leakage in the frequency domain most dramatically. Nevertheless, the effect is always present and energy will leak out from the signal frequency bin present. This can be seen in figure 2.8. If the input signal frequency is a multiple of f_{res}, the monofrequent signal will show up only in one frequency-bins. Or short:"... any input signal whose frequency is not exactly at a DFT bin center to leak into all of the other DFT output bins." ***Spectral leakage*** (or short 'leakage') can not be avoided, and will alter the results in the frequency-domain. Please note that the amplitude in the according frequency bin is changed dramatically by leakage. Figure 2.7 gives an example for leakage on a 64 point DFT.

Figure 2.8 shows the effect of sampling. Looking at the result of the DFT frequency of 10 kHz, we have recorded an exact delta-peak with no unwanted side peaks in the sampled frequency data, although the effect is present as can be seen from the CFT data in the background. The DFT of 10.5 kHz results in two peaks at 10kHz and 11kHz and further unwanted side peaks called side lobes. Those side lobes, that "roll off" from the main peak corrupt neighbour frequency bins, especially when they are of low-level amplitude. The amplitude of the side lobes, when using a rectangular window, decreases fast with the windows size, but they "roll off" very wide. The same problem can also be seen in figure 2.2. The FT of a window function is the absolute value of the ***sinus cardinalis (sinc)*** $(sin(x)/x)$, which is convoluted with the delta function of the single frequency signal.

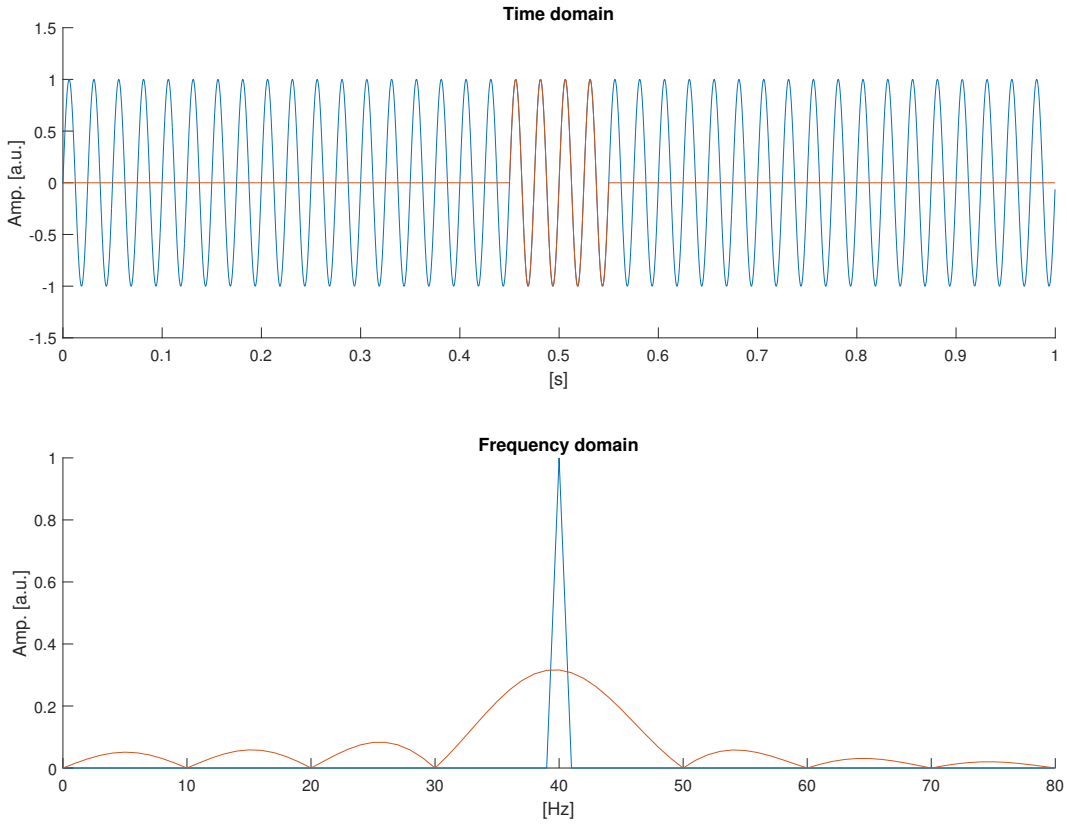

Figure 2.6: Spectral leakage on a windowed time signal [19]

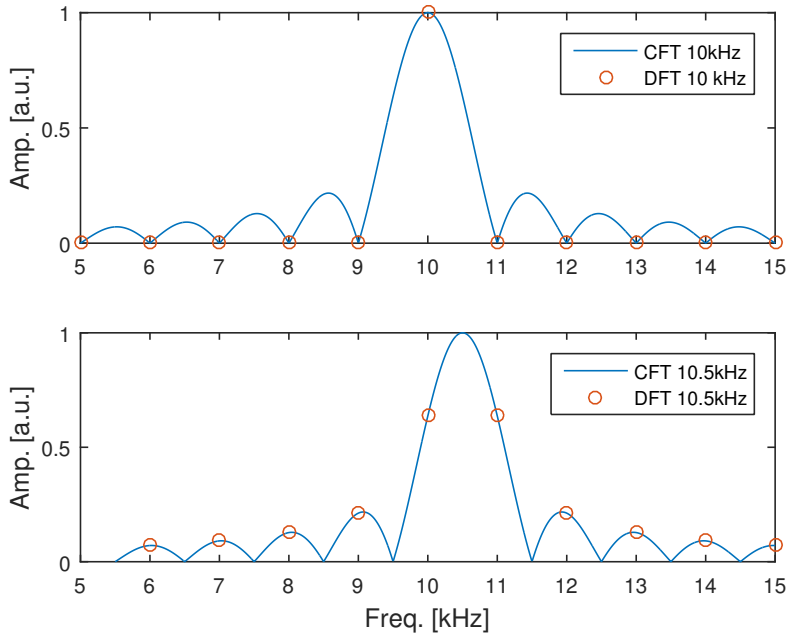

Figure 2.8: Leakage in CFT and DFT at 10 and 10.5 kHz

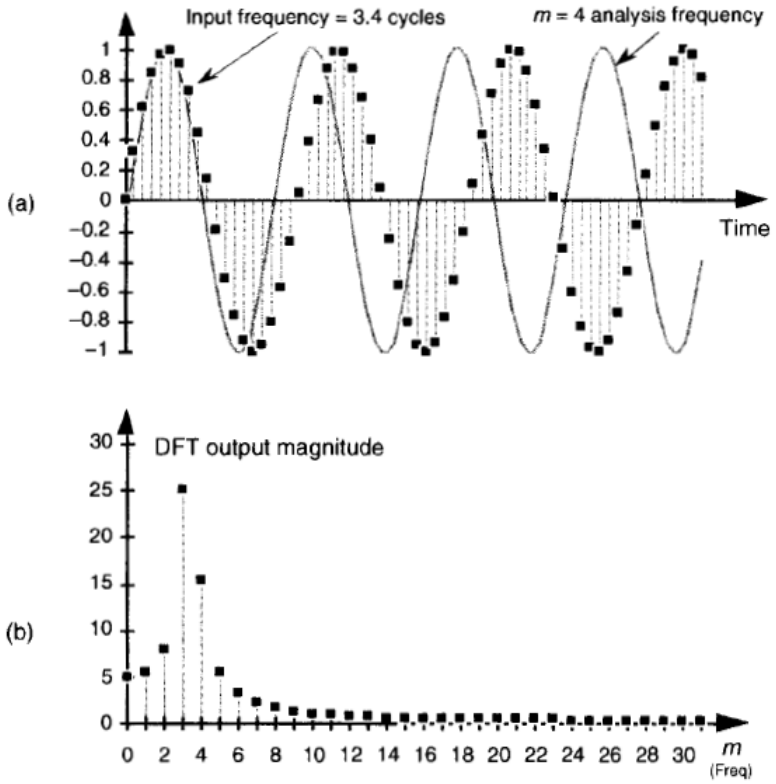

Figure 2.7: Spectral leakage on a 64-point DFT [19]

To reduce the effects of leakage, the most common remedy is ***windowing***. As Harris stated: "Sampling is well understood, windowing is less so, and sampled windows for DFT's significantly less so!" [22]. In this thesis windowing of the time domain samples will be discussed. It is worth mentioning that windowing also provides further abilities. For example the flattop window, results in excellent amplitude accuracy, when single frequency signals are sampled.

As we see in figure 2.8 the FFT of a sine-wave, which in our case is multiplied by a rectangular window, is the sinc function in the frequency domain. The rectangular window is the standard or uniform window always present when no other window is applied.

Taking a look at 2.9 shows us the impact of different window functions on the DFT.

Windowing reduces the magnitude of the side-lobes of the sinc function, which cause the leakage effect. Taking in consideration Parseval's Theorem, equation 2.2.3, we can see that the leakage effect also decreases our main amplitude. This can be seen in figure 2.9 in the amplitudes of the rectangular and hanning spectrum of the time signal. For equation 2.2.3 the windowed time signal has to be used to be fulfilled.

The window-function has the same length as our discrete data set of the SL. Those windows reduce the side lobes by forcing the magnitudes at the beginning and the end of the time domain sample to a single common amplitude value, usually 0. [19].

Since our signal in figure 2.9 has 24.4 Hz, with 1Hz f_{res}, it will cause a peak in the 24Hz bin and the 25Hz bin. Comparing the frequency domain of the hanning window and the rectangular window in figure 2.9, the side lobes in the hanning window decrease faster. Hence corruption of low level amplitudes in its closer neighbourhood will not occur. Taking a look at the amplitude values, the flattop window, figure 2.9 bottom right, returns accurate values in both frequency bins, 24 Hz and 25Hz, though the signal frequency is 24.4Hz.

So we can resume:

- The hanning window suppresses the effect of leakage better than the flattop or the rectangular window.
- The flattop window does not suppress the effect of leakage, but derives us excellent amplitude values.

To retrieve the amplitude of a windowed DFT from pwelch(), it has to be multiplied by the ***Equivalent Noise Band Width (ENBW)***, since the window function acts like a filter. The ENBW is the ratio between the squared average of the power of a signal after an ideal filter, which is represented through the rectangular window (sometimes referred as brick-wall-filter) and the squared average of the power after windowing. The testing signal is white noise (energy at all frequencies).

Since the Matlab command enbw() returns the ***normalized equivalent noise bandwith NENBW***, it has to be scaled by the ratio SR/SL, if f_{res} was not chosen as 1Hz to retrieve the ENBW. The ENBW is than multiplied with the PSD and we receive the PS.

The ENBW can also be calculated by equation 2.2.6, where f_{res} is allready considered.

$$ENBW = SR \, \frac{\sum window^2}{(\sum window)^2} \tag{2.2.6}$$

An overview on further filters and their abilities can be seen in table 2.1.

Examples for FFT routines in Matlab can be found in Appendix A.3 for a single signal.

For calculation of CPSD an example can be found in Appendix A.4.

Table 2.1: Overview on window functions [45]

Window	***Signal Content***
Hann	Sine wave or combination of sine waves
Flat Top	Sine wave (amplitude accuracy is important)
Hann	Narrowband random signal (vibration data)
Uniform	Broadband random (white noise)
Uniform, Hamming	Closely spaced sine waves
Force	Excitation signals (hammer blow)
Exponential	Response signals
Hann	Unknown content
Hann	Sine wave or combination of sine waves
Kaiser Bessel	Two tones with frequencies close but amplitudes very different
Uniform	Two tones with frequencies close and almost equal amplitudes
Flat Top	Accurate single tone amplitude measurements

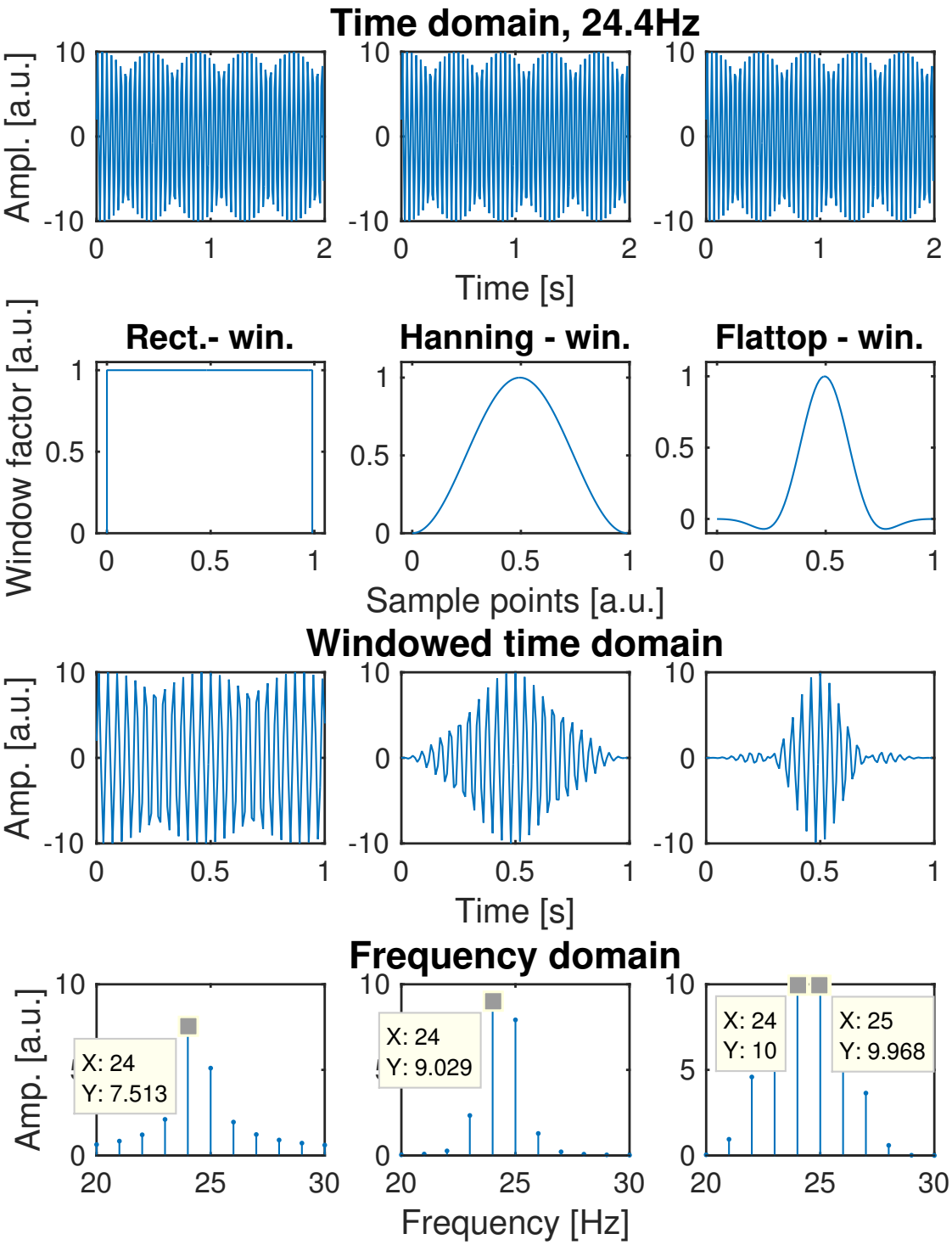

Figure 2.9: Example for windowing and its effect on a sine wave with 24.4Hz and amplitude of 10

2.3 Experimental Setup

This section presents the basic experimental setup used in different experiments. Certain adaptations have been made for the different experiments and will be described in detail.

The laboratory is located in the basement, where a direct connection to the ground is given and no vibrations from the building (e.g. compressor station) can be transferred on the setup.

The basic setup can be seen in figure 2.10 and will be described in the following. The exact equipment specifications and set values can be found at the end of this section in table 2.3.

The experimental burner is placed in a cabinet $3m \times 3m \times 2.5m$ surrounded by two layers of theatre curtains, which absorb acoustic noise and are fire-resistant. For the ceiling, noise absorbing panels are used. The exhaust fumes get extracted through a expulsion system in the ceiling.

The experiments in this thesis were performed on a 3.4 kW unconfined, swirl-stabilized, methane-fired burner with a detached flame under ambient conditions. The experimental burner was designed by T. Leitgeb [30]. Further documentation on the burner can be found in detail by Giuliani et al. [31]. The rotational symmetry of the flame was shown by Peterleithner et al. [46]. The burner can be operated with methane gas either ***technically premixed (TPM)*** or ***perfectly premixed (PPM)***. In the TPM case methane and air were mixed in the burner. For PPM methane was premixed in an separated mixing chamber with the tangential air. 32 tangential bores in 4 rows injected the mixture. Thus a rotational symmetric flame was obtained. Due to a better flame stability in operation and therefore less noise in the signal, PPM conditions were chosen.

During the thesis a radiation measurement with a thermopile was performed, which resulted in $190W$. Hence the heat release by radiation (5.5%) of equation A.2.5 was neglected.

Methane was taken from a gas bottle, passed through a pressure reducer, a calibrated mass flow sensor with a valve and then got mixed with the air. Then a sirene modulated the gas flow. Since the plenum resonance was close to 212Hz, this frequency was chosen for the ***sirene*** excitation to obtain a good signal in the flame. The sirene basically consists of a turning chopper disc, chopping the axial mass flow of the gas at a frequency of 212 Hz. The 212 Hz signal from the sirene was recorded as well. Further information on the siren can be found in [47].

The burner was mounted on a 3 component ***traversing unit*** and was moved three axis X,Y, and Z. This traversing unit was powered by a controller, which was connected to a PC. On the PC the traversing unit was controlled via a LabView 2012 routine.

The ***Laser interferometric vibrometer*** was fixed on a pillar. In front of the LIV a diverging ***lense (L)*** with -40 mm focal length was mounted for collimating the beam to a parallel beam of light with 2 or 5 mm diameter. This beam was then reflected by a ***front surface mirror*** back into the LIV. The mirror is mounted 1.65 m away from the end of the LIV- lense.

For reference measurement a condenser ***microphone*** was mounted on the burner.

Behind the burner a ***photo-multiplier*** with an OH*-filter collected the ultraviolet radiation at 306 nm, so fluctuations of heat release can be measured by chemiluminescence for reference.

The four signals from the siren, LIV, microphone and photo-multiplier are then sampled by an ***analog-digital (A/D) - converter***. The SR was set to $16384S/s$ and the signals were recorded for a time

period of 60 seconds. When different SR and recording times were used, it will be noted the results section 3.

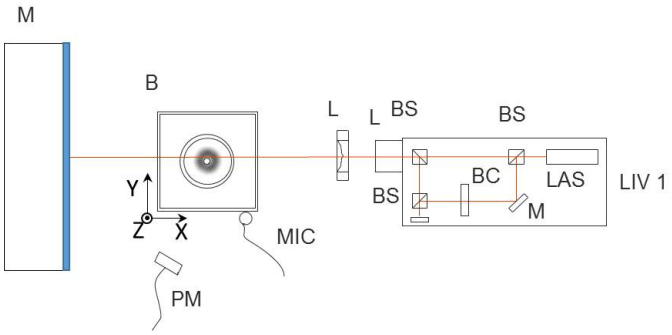

Figure 2.10: Basic experimental setup with BS - Beam splitter, BC - Bragg cell and LAS - Laser

To verify Strahles equation, the sound filed was recorded with a setup seen in figure 2.11. Due to the long wavelength of $1.6m$ the measurement was done in the acoustic near field. Therefore ***pressure-pressure (PP)*** probes were used to retrieve the ***sound intensity (I)*** of the flame. PP-probes consist of two microphones facing each other, with a fixed distance of 52 mm and can be seen in figure 2.11 in the blue circle. The 14 PP-probes are then mounted equidistant in an array on a bow with a radius of 1013 mm. One additional microphone was needed at a distance of 200 mm for reference. Before usage, the microphones were calibrated in a pistonphone at a frequency of 250 Hz with a volume of 114 dB(linear) / 105.4 dB(A). The analog signal from the microphones was then amplified and passed to an A/D converter. The A/D converter is connected to its own computer via fiber optic due to the big volume of data.

With the data received from this measurement, sound intensity was calculated and thus the ***sound power (P)*** for a hemisphere as reference for the LIV measurement in the flame can be calculated. (see equation 2.1.14.

Following equation 2.3.1 shows that pressure measured from the two microphones p_r and $p_{r+\Delta r}$ opposing each other can be related to the sound intensity, whereas Δr represents the distances between the two microphones [34]:

$$I_r = p' v_r = -\frac{p_{r+\Delta r} + p_r}{2} \frac{1}{\rho} \int_t \frac{p_{r+\Delta r} - p_r}{\Delta r} dt \tag{2.3.1}$$

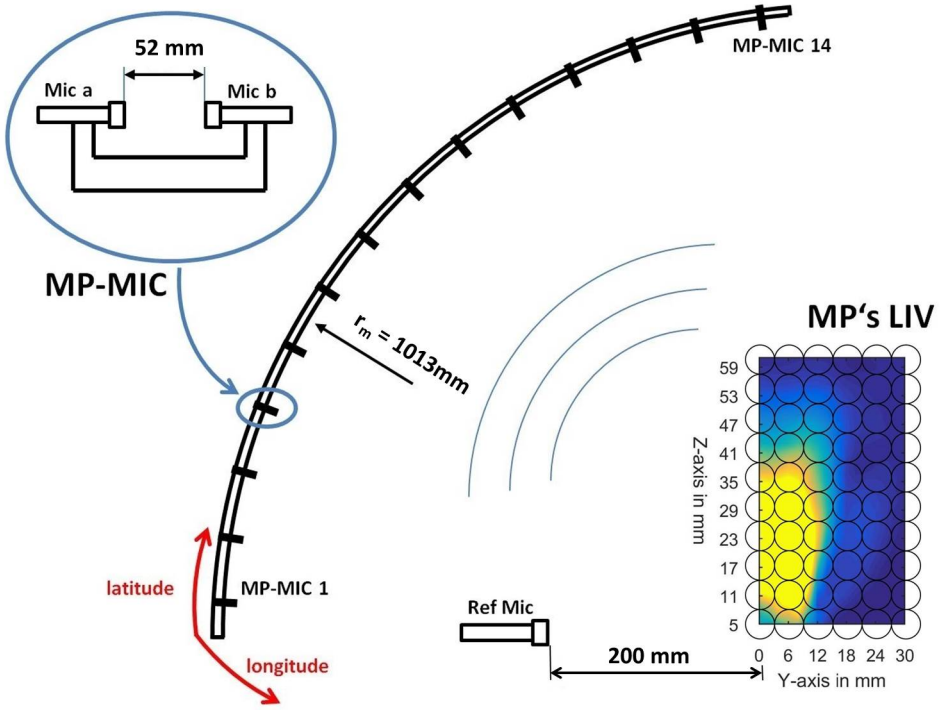

Figure 2.11: Microphone array and field of LIV Measurement Points (MP's)

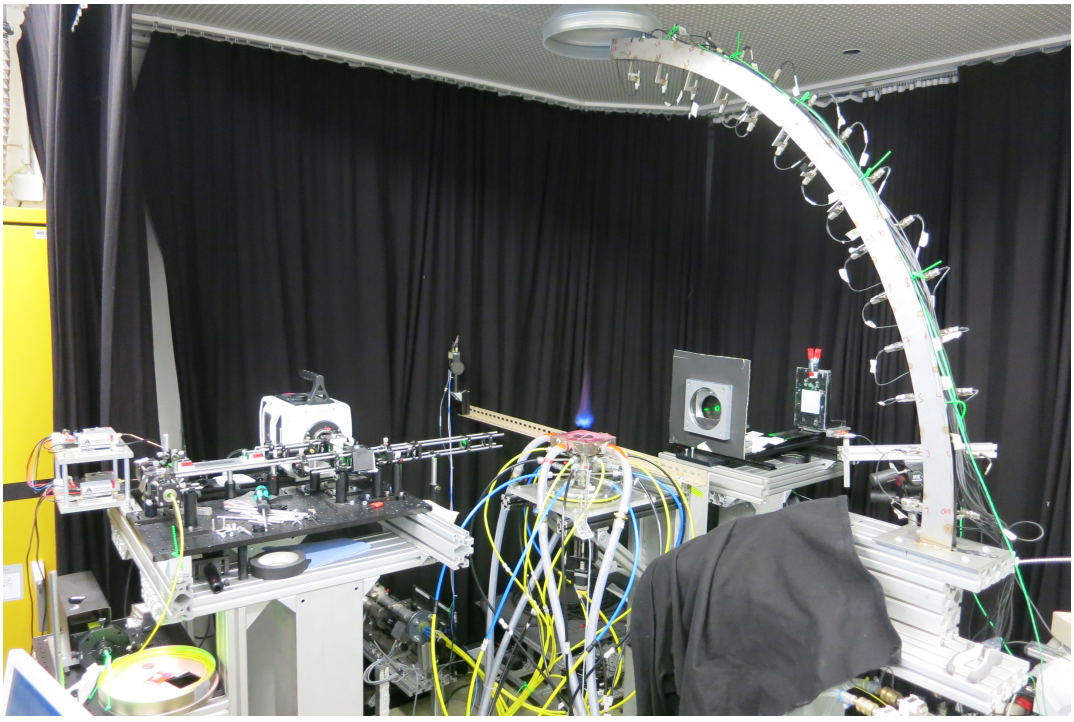

Figure 2.12: Setup with acoustic array and Full Field Laser Interferometric Vibrometer (FFLIV) developed at TU Dresden

In order to record the sound field emitted by the flame, a reference measurement was performed, using a ***loud speaker***. For measuring the sound-waves, two mirrors and an additional traverse were used. The setup can be seen in figure 2.13. A ***signal generator*** with an ***amplifier*** was used to drive the loud speaker.

Measurements showed, that the influence of reflections in the sound field were too big to obtain trustworthy results. Thus the ***reverberation time*** RT_{60} was measured with an audio analyser. Afterwards 27 sound absorbing foam panels with a size of $62 \times 50 \times 10cm$ were mounted in a channel profile in front of the sound source. Then the RT_{60} was measured again. With the Sabine equation 2.3.2 the ***critical distance*** d_c could be calculated. Whereas V represents the volume of the measured room in meters. If the distance from the sound source is bigger than d_c, reflections are dominant, vice versa the signal from the source is dominant.

$$d_c = \sqrt{\frac{V}{100\pi\ RT_{60}}} \tag{2.3.2}$$

As it can be seen in table 2.2 the absorbing panels enhanced the measurement distance more than 30%.

Table 2.2: RT_{60} measurement results

	$RT_{60}[s]$	d_c [m]
250 Hz, no absorber	0.40	0.36
1000 Hz, no absorber	0.16	0.57
250 Hz, with absorber	0.24	0.47
1000 Hz, with absorber	0.15	0.59

Since the frequency of the signal-generator drifted slowly in phase a second LIV, LIV 2, was mounted behind the mirrors, focused on the membrane of the speaker. LIV 1 was mounted on a bigger ***traversing unit***, since the traverse of the burner provided only $400mm$ of traversing. The bigger traverse unit had $1000mm$ range. The axis of the bigger traverse unit, Y', was mounted parallel to the Y-axis of the burner's traverse started close to the origin of the burner. The whole setup can be seen in figure 2.13. This bigger traverse unit was powered by a controller, which was connected to a PC and was controlled via a LabView 2012 routine.

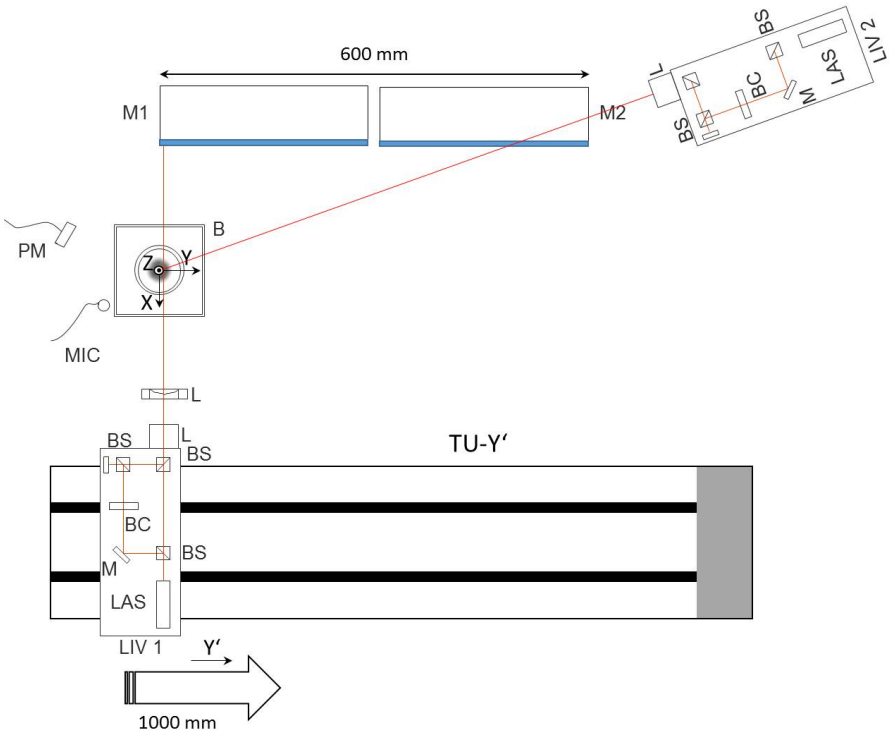

Figure 2.13: Experimental setup for LIV measurement, M1 - Mirror 1, M2 - Mirror 2, L - Lens, B - Burner, PM - Photo multiplier, MIC - Microphone, BS - Beam splitter, BC - Bragg cell, LAS - Laser, LIV - Laser Interferometric Vibrometer

Table 2.3: Specifications of the used equipment

Equipment	***Specification***	***Set values***
Analog digital converter	National Instruments - NI 9215(A) with BNC - Austin, Texas	16382 S/s, 60 seconds
LIV 1	Polytec - OFV-MR-503 - Waldbronn, Germany	-
LIV 1 controller	Polytec - OFV-5000 Vibrometer Controller - Waldbronn, Germany	$k_{vib}1mm/s/V$, $20kHz$ bandwith, no filters
LIV 2	Polytec - OFV-353 - Waldbronn, Germany	-
LIV 2 - controller	Polytec - OFV 3001 - Waldbronn, Germany	$k_{vib}125mm/s/V$, $1.5MHz$ bandwith, no filters
Sirene	TTM institute - custom-built - Graz, Austria	212 Hz, baudrate 115200 timeout 500 ms
Photo-multiplier	Thorlabs - PMM01 - Newton, New Jersey	-
Microphone	TTM institute - condenser microphone with custom amplifier - Graz, Austria	-
Traversing unit	Dantec Dynamics - leight weight traversing unit - Roskilde, Denmark	-
Traversing unit controller	ISEL - C 10C - Eichenzell, Germany	9600 baudrate
Big traversing unit	ISEL - LES5 1090 - Eichenzell, Germany	-
Big traversing unit controller	ISEL - iMC-S8 - Eichenzell, Germany	baudrate 19200
Signal generator	Voltcraft - FG 708S - Hierschau, Germany	1.06 V for 1000 Hz and 212 Hz
Amplifier	Monacor - PA-400 - Bremen, Germany	6 a.u.
Mass flow sensors	Bronkhorst - EL-FLOW series - Ruurlo, Netherlands	For perfectly premixed: Methane 0.0682 g/s, tangential air 0.397 g/s, axial air 0.422 g/s, cooling air 0.969 g/s
Thermopile	Kipp&Zonen - CA 2 Laboratory Thermopile - Delft, Netherland	sensitivity 1 $19.1\mu V/W/m^2$, sensitivity 2 $0.053\mu V/W/m^2$
Microphones	G.R.A.S. Sound & Vibration- 40BD 1/4", prepolarized pressure microphone - Holte, Denmark	-
Pistonphone	G.R.A.S. Sound & Vibration - Type 42AA - Holte, Denmark	-
Microphone amplifier	G.R.A.S. Sound & Vibration - Power Module 12AN - Holte, Denmark	-
Microphone analog digital converter	National Instruments - NI PXIe 1062Q - Austin, Texas	100kS, 30s
Lense	Spindler & Hoyer - f-40 plano-concave lense- Göttingen, Germany	-
Speaker	Conrad Electronics - Speaka special Nr. 30 1995- 8 Ohm, 25W, 90-17000 Hz - Hirschau, Germany	-
Audio analyser	NTI Audio AG - XL 2 - Handheld audio and acoustic analyzer - Schaan, Liechtenstein	RNG 20 - 120
Audio analyser microphone	NTI Audio AG - MA220 - Schaan, Liechtenstein	-
Acoustic panels	Lambda Labs - Polyesterfiberboards - $62 \times 50 \times 10cm$ - $40kg/m^3$, Austria	-

3 Results and Discussions

3.1 Measurement of Sound Power Emitted by a Swirl-Stabilized Flame

The objective of this thesis was to verify the capability of LIV to determine heat release fluctuations and sound emission from a flame quantitatively. Therefore the data evaluation routines were optimized by the author and former measurements performed by Greiffenhagen et al. [34] were validated and compared to new recordings done during this thesis work. This included the recording of the sound power emitted by the flame. This sound power was measured by microphone arrays to retrieve information about the relation to the density fluctuations – recorded by LIV – and compared to the theory provided by Strahle [8] (see section 2.1, equation 2.1.13). The operating conditions of the flame are given in table 3.1. A perfectly-premixed flame condition was choosen for all these experiments to avoid so-called lamda-waves, variations in the fuel-to-air ratio during the heat relaese fluctuations. These variations cause non-linear effects in the OH* emission, thus over- or underestimating the heat fluctuations in the chemiluminescence signal [48]. All recordings were evaluated for a frequency of 212Hz excited by the siren. Sampling frequency was 100kS/s, SL 100kS, frequency resolution 1Hz, sampling time was 30s. For windowing a uniform (rectangular) window was choosen, due to the signal characteristic (siren excitation with strong side bands and overtones and the discussion from table 2.1)

Table 3.1: Operating conditions of the perfectly premixed atmospheric swirl-stabilized methane flame

$\dot{m}_{ax}$ $[g/s]$	$\dot{m}_{tan}$ $[g/s]$	$\dot{m}_{cool}$ $[g/s]$	$\dot{m}_{fuel}$ $[g/s]$	ϕ_{global} $[-]$	P_{th} $[kW]$
0.424	0.378	0.969	0.068	0.66	3.44

Peterleithner et al. [10] proved the rotational symmetry of the flame, thus sound power measurements have been performed during this thesis to determine the influence of reflections and acoustic refraction in the cabinet. Therefore the burner was rotated around the Z-axis from $-90°$ to $+90°$ in 9 increments, each $22.5°$. The microphone array shown in figure 3.7 and 2.3 recorded a full data set along the arch. Figure 3.1 shows the angular distribution of the total sound power (integral along the arch) in % of the average value.

Since rotational symmetry of the flame is assumed and was proofed, the deviation in sound power can be used to characterize the measurement error of the acoustic measurement. Reflections are suspected to be the main source of disturbance. The standard deviation of the sound power in figure 3.1 is $\pm 5.61\%$, thus the results from acoustic measurements are within the reliability of the rotational symmetry of the flame [46] and therefore can be assumed as accurate enough for a comparison of LIV and microphone data. Thus Abel transform, which is used to obtain locally resolved data, will yield accurate results. In future experiments a cabinet with sound absorbing panels for low frequencies should be used to reduce the effect of reflections and yield results with higher accuracy. A detailed plot of the sound intensity in different directions is shown in figure 3.2 together with the averaged data along the arch segment. The sound intensity is related to the sound power via the area and is given in arbitrary units in figure 3.2 in order to compare non-uniformities in sound emission.

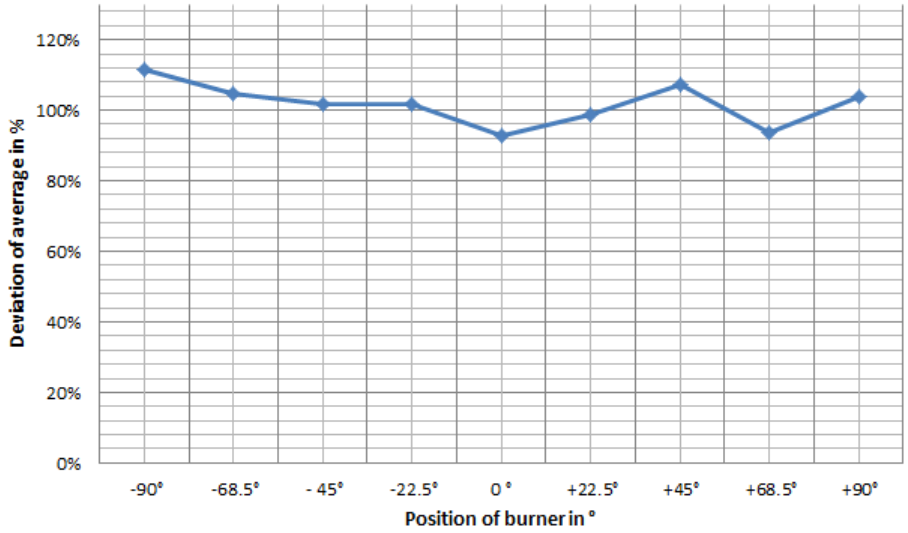

Figure 3.1: Angular sound power distribution

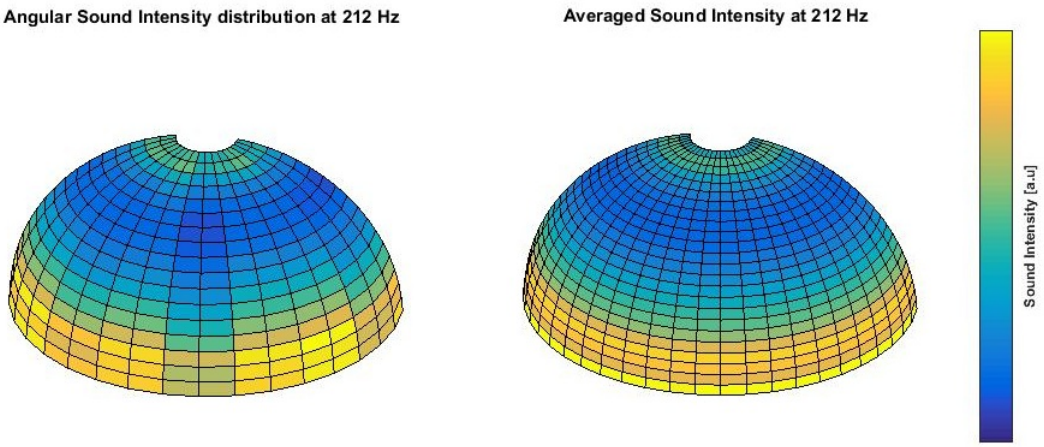

Figure 3.2: Sound Intensity distribution at 212 Hz, measured with the microphone array. Left: detailed recording for -90° to +90° flame rotation. Right: averaged data for all positions along the arch.

In order to compare microphone data with heat release fluctuations using equations 2.1.13 and 2.1.14 a LIV measurement of the flame was performed and resulted in the density fluctuations in the flame $d\rho'_T/dt$ (see equation 2.1.9). The measurement array consisted of $16 \times 2mm$ measurement points in Y (radial) direction and $58 \times 2mm$ measurement points in the Z (axial) direction with a beam diameter of 2 mm (see figure 2.11 for the measurement array).

Additionally a field scan with 5 mm distance between scanning points was also performed for this thesis.

Both fields are compared in figure 3.3. Sample frequency was 16384S/s first SL 16384S (1Hz resolution) and for the final evaluation SL 163840S (1/10Hz resolution). This change was due to the fact, that long samples and uniform (rectangular) windowing reduces spectral leakage in this type of signal and provides amplitudes with higher accuracy (see section 2.2.2). Since less information was available on the 5 mm grid, the information from the 2 mm beam gets spread on a 5 mm cell, which resulted in the loss of information and resolution. Thus the result is not trustworthy.

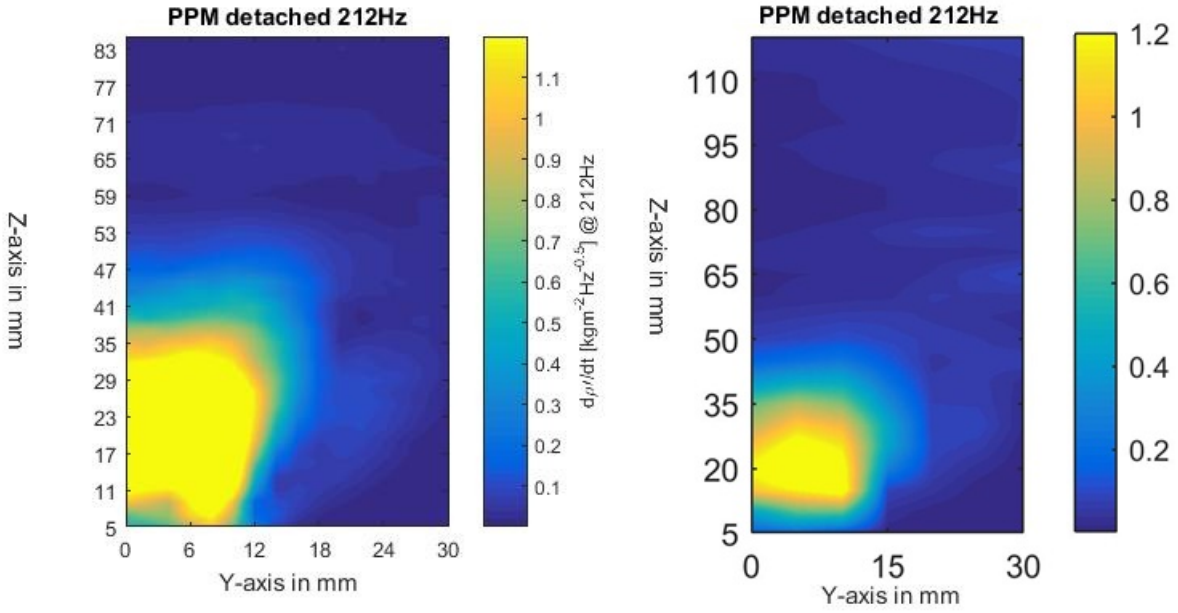

Figure 3.3: Radial distribution of density fluctuations (line-of-sight data). A correction with the local Gladstone-Dale constants (provided by F. Greiffenhagen) was performed. Left: 2mm grid with 2mm laser beam diameter, right 5mm grid with 2mm laser beam diameter.

Applying equation 2.1.13, the sound power can be calculated from density fluctuations in the flame. The corresponding frequency resolved power spectrum is plotted in figure 3.4. The LIV predicts a total sound power $P_{total,LIV} = 3.24 * 10^{-}6W$ at 212 Hz and the total sound power recorded by the microphone array is $P_{total,microphones} = 3.77 * 10^{-}6W$ at 212 Hz which is in good agreement and proofs Strahles assumption.

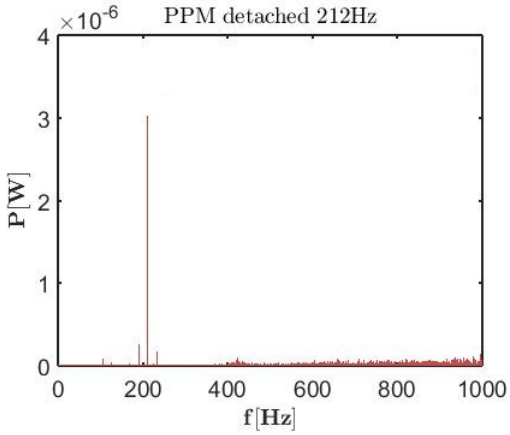

Figure 3.4: Frequency resolved sound power distribution from LIV measurement

Considering that one LIV measurement consists of 928 scanning positions and the complete scan takes approximately 18 hours [1] the microphone recordings were taken quasi-simultaneously. After scanning two lines with the LIV one recording with the microphones along the arch was performed. At the end all microphone readings were averaged. Thus, long term fluctuations of the burner were averaged out.

Strahle assumes the flame to be an oscillating monopole [8]. From density recordings the phase of oscillation can be plotted for each radial and axial position. Local phase information can be obtained from a cross correlation between the siren and LIV signal, using the CPSD algorithm presented in section 2.2.1. Since the combustion process is highly turbulent, a large number of spectra has to be averaged to provide a meaningful result. The single phasors recorded from a set of FFT spectra in various positions are plotted in figure 3.5. The larger the turbulent variations are, the larger the number of samples have to be, to result in a meaningful average phase for this position (theory of confidence intervals for a meaningful mean from turbulent data). Furthermore a strong correlation of the LIV signal up to $930mm$ in radial distance from the flame can be seen in figure 3.5.

[1] In an ongoing research project with the TU Dresden a high speed camera is used as sensor and therefore multiple measurement points can be captured in a single take. Hence the measurement time will be reduced considerably.

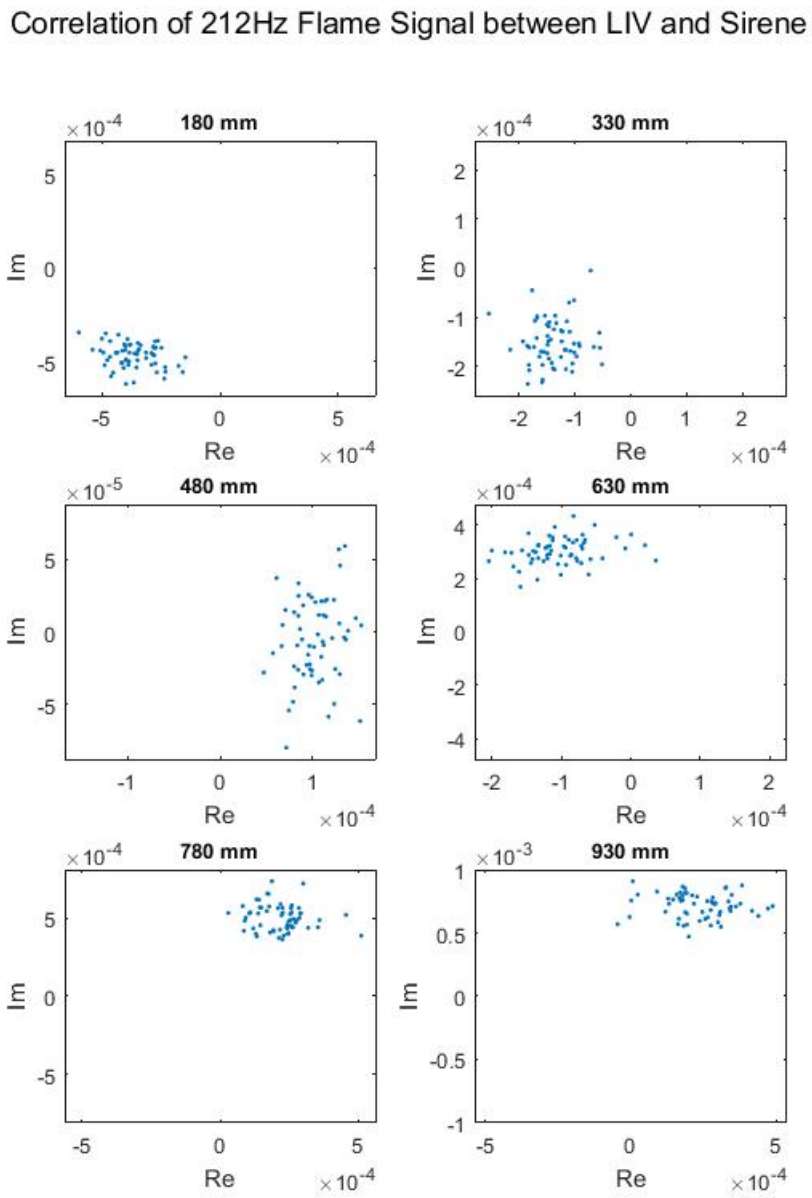

Figure 3.5: Phasors for various positions scanned. The phasors are from the correlation of LIV and siren data at 212Hz.

From figure 3.6 it can be seen, that the flame consists of various oscillations - phase shifted lobes with a wavelength of approximately 16mm due to the flow velocity and the 212Hz oscillations in the flame. Thus, the wavelength of the local density oscillations (caused by convection) is much, much smaller than the wavelength of the sound emitted at 212Hz (approximately 1.6m at ambient conditions). This is in agreement with Strahles assumption that the flame acts as oscillating monopole for sound emission at low frequencies.

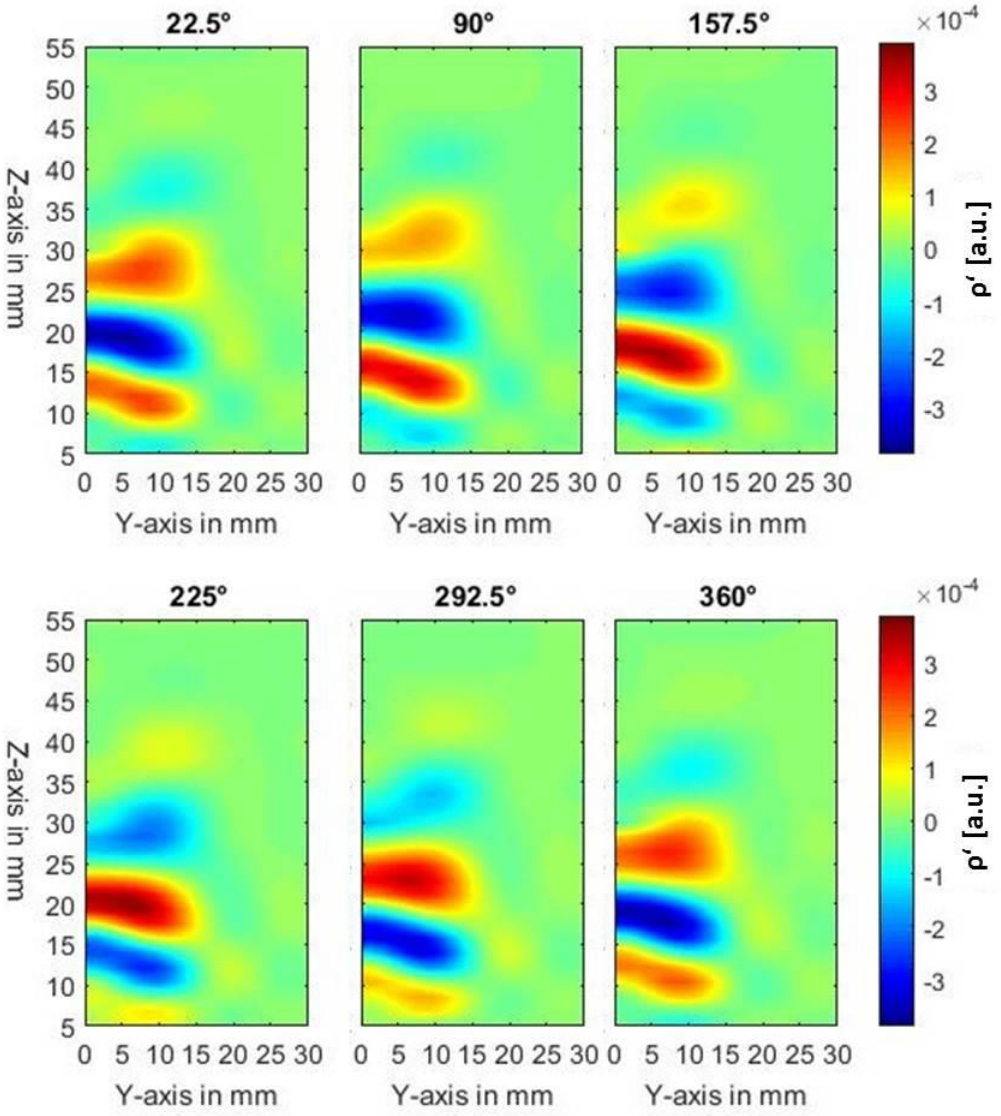

Figure 3.6: Phase resolved local density fluctuations at 212Hz along the jet axis Z, and the radial direction Y

From the microphone recordings plotted in figure 3.2 we learn, that the sound emission is not uniform in all direction. A possible reason for this behaviour is the influence of the temperature and velocity field on the sound emissions from the oscillating flame, which results in a refraction of the sound field [8]. Therefore a measurement of the sound field outside the combustion zone with the LIV according to equation 2.1.11 could clear this question.

3.2 Measurement of Acoustic Emissions of a Speaker via LIV

To prove the capability of the LIV to measure the sound field emitted by the flame at 212 Hz, the measurement was done using a sound speaker. This speaker provides the possibility to produce a mono frequent signal, which can be controlled via a frequency generator and an amplifier, thus achieving repeatable results. The sound speaker is a well suited acoustic source to optimize and validate the measurement procedure. Similar experiments have been performed earlier by [5] [6] [7].

Measuring sound waves at low frequencies (212 Hz) and intensities can be difficult due to various reasons. Foremost low frequency sound waves do not couple into the curtains surrounding the flame at a distance of 1.5m in the cabinet as desired. Therefore interference with the reflected sound waves occurs and only a noisy signal can be attained through measurement.

Thus a gradual approach was chosen, to eliminate errors and improve the signal to noise ratio. For that purpose a first measurement was performed at 1000 Hz, at this frequency the curtains have a good absorption behaviour. The second frequency was 212 Hz. The sound waves were measured via LIV, using the relation between voltage and pressure seen in equation 2.1.11 and was then presented in single plots using the real part of the CPSD (see section 2.2.1).

The measurement array included 51 positions with a distance of 20 mm in Y direction and 5 positions with a distance of 20 mm in Z-direction for the 1000 Hz field. This is seen schematically in figure 3.7. It must be noted that LIV integrates over line-of-sight and no Abel transform was performed. This means that for the numerical simulation which was done to better understand the LIV data such an integration of the field data had also to be performed.

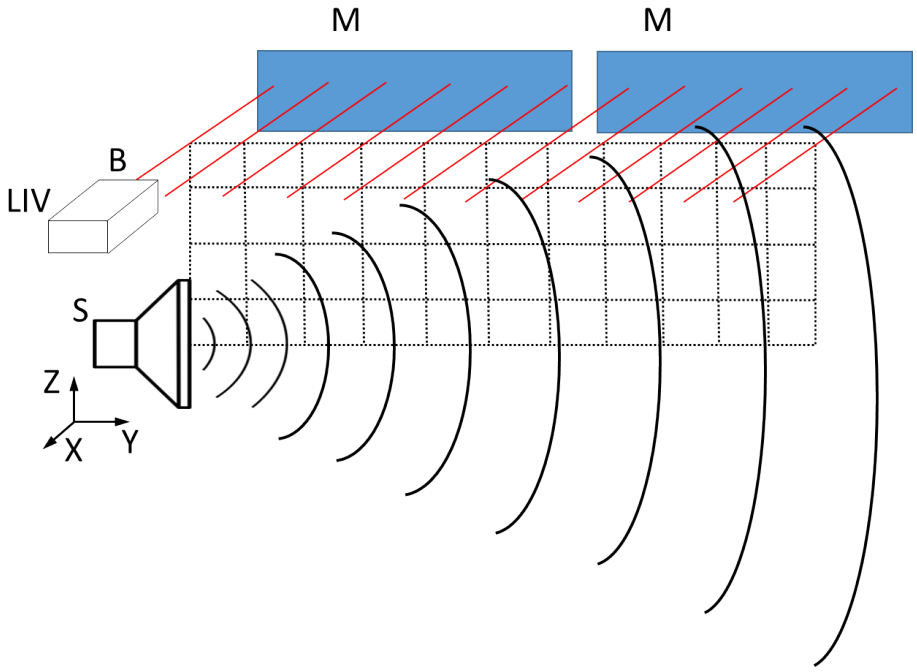

Figure 3.7: Schematic array of measurement points with coordinate system, speaker (S), laser beam (B), mirrors (M), (LIV) Laser Interferometric Vibrometer

The results of the 1000 Hz measurement can be seen in figure 3.8. As phase reference, the signal from a second LIV was used, pointing towards the speaker membrane with a retro-reflective foil attached to this surface to improve the signal-to-noise ratio. The top plot shows the integral values of the sound field in collinear with the beam of the LIV, and therefore represents line-of-sight data (integration along X-axis). The bottom plot shows the total integral value of the sound field (integration in X and Z-direction).

For a better understanding of the results, a simple simulation in Matlab was written, using spherical waves emitted by the surface of the speaker in various positions along the membrane. This code can be found in appendix A.5. The results of the simulation can be seen in figure 3.9.

When comparing figure 3.8 with figure 3.9 there is basic agreement with various differences which may be caused to following uncertainties in the experimental setup:

- Reflections of the sound waves from surrounding equipment
- Malfunction or no proper setup of the equipment
- Different characteristic of the sound emission (other than spherical)

Taking the critical distance d_c for acoustic reflections in consideration (see 2.3), more than 50 cm away from the speaker in radial distance, deviations between the measurement in figure 3.8 and the simulation in figure 3.9 become evident. Thus only the radial distance from the speaker approximately up to 50 cm can be assumed accurate enough. Comparing simulation and measurement, it must also be taken in account, that the emission characteristic of a speaker is not spherical and cancellation axes are observed (see figure 3.6).

While for $1000Hz$ the absorption of the doubled curtains was sufficient, this was not the case for the 212Hz frequency. A low d_c at that low frequency and various failed attempts to measure the sound field at 212 Hz, resulted in an enhancement of the cabinet with acoustic absorber plates and an audio analyzer from the Signal Processing and Speech Communication Laboratory. By mounting the panels in tunnel shape, as it can be seen in figure 3.11, it was tried to improve the acoustic absorption in the cell and avoid reflections from the aluminium pillars supporting the experimental setup.

The absorption coefficient for porous acoustic materials can be seen in figure 3.12. Most of the absorbing panels have a steep drop in the area of 100 to $900Hz$. Hence the measurement of the reverberation time at $250Hz$ may be inaccurate for measurements at $212Hz$, since a lower absorption coefficient α yields in higher transmission and reflections coefficients.

Regarding equation 2.3.2, removing the acoustic tunnel will increase the reverberation time but increases the volume of the measurement room and leads to higher d_c. Additionally, mounting the absorber panels in a non-uniform, "chaotic" pattern gives more edges for refraction of sound. It must be kept in mind, that the best absorption can be achieved when the panel have a thickness of ¼ of the wavelength under investigation. This means that for the 212Hz frequency four panels must be piled one behind the other, to have an approximately 400 mm thick panel. Therefore several fields with various configurations of the panels were sampled for the 212Hz frequency. The results are discussed in the following sections.

Figure 3.13 plots the sound simulation at 212Hz with spherical waves emitted from the surface. The

results of the measurement with the damped tunnel (figure 3.11) can be seen in 3.15. Severe reflections can be seen between 300 and 400 mm in radial direction from the center of the speaker. These reflection might be due to the uncovered pillars supporting the setup, the mirrors and the ISEL traverse used to traverse the LIV system.

In a next step, the absorbers were arranged non-uniform all over the place, to avoid direct reflection from the pillars. The result can be seen in figure 3.15 already cut down to a d_c of 300 mm.

Due to this low d_c value in the 212Hz measurement, the ISEL traversing unit and its mounts were removed, since these objects are made out of aluminium and present rigid and highly reflective surfaces. This was also possible since traversing the LIV only for 300 mm can also be done by traversing the sound speaker for 300 mm on the traverse used to traverse the burner. This smaller traversing unit (Dantec) was then used to record a sound field as it can be seen in figure 3.16. This result is assumed to be the most accurate possible with the current setup. For an enhancement of the results, further modifications are needed, for example an anechoic chamber, coarse concrete blocks, or low frequency absorbers like Helmholtz resonators (see [50], chapter 12). It should be pointed out, that even a measurement in a better environment can not assure a non-disturbed distribution of the sound waves due to the difficulty of absorption at low frequencies and strong reflections at the LIV measurement setup and the burner it self.

Additionally the results in the figures 3.14, 3.15, 3.16, do not fit with the simulation. This can be explained with the radial distance r from the speaker, not fulfilling the condition $r \gg \lambda$, with the wavelength λ. Thus the measured field is settled in the near field of the source and more advanced simulations which take the mass spring interaction of the air in consideration should be performed (see [51]).

When comparing the results from the simulations with the experimental data at $1000Hz$ and $212Hz$, the miss of an equal distributed sound field can be explained due to different emission characteristics used for the basic simulation. Looking at the plot in figure 3.16, the directional characteristics of the speaker seem to be characterised by one main lobe in the middle and two side lobes. This is a very common assumption, found in literature and also through experiments [49]. It can be also seen in the experimental data recorded by LIV.

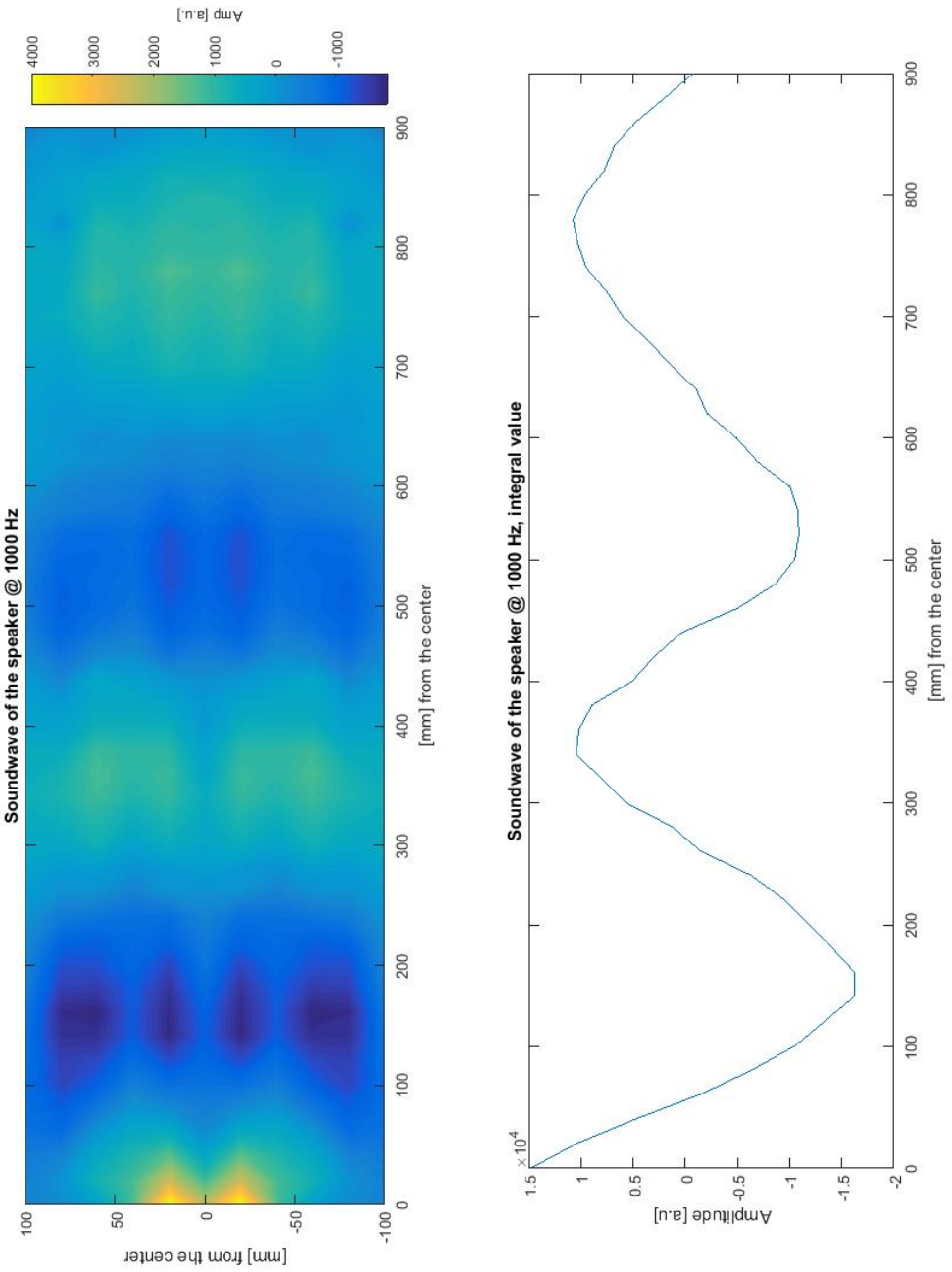

Figure 3.8: Sound field at 1000 Hz, integral values in X-direction top, integral values in X,Z-direction bottom

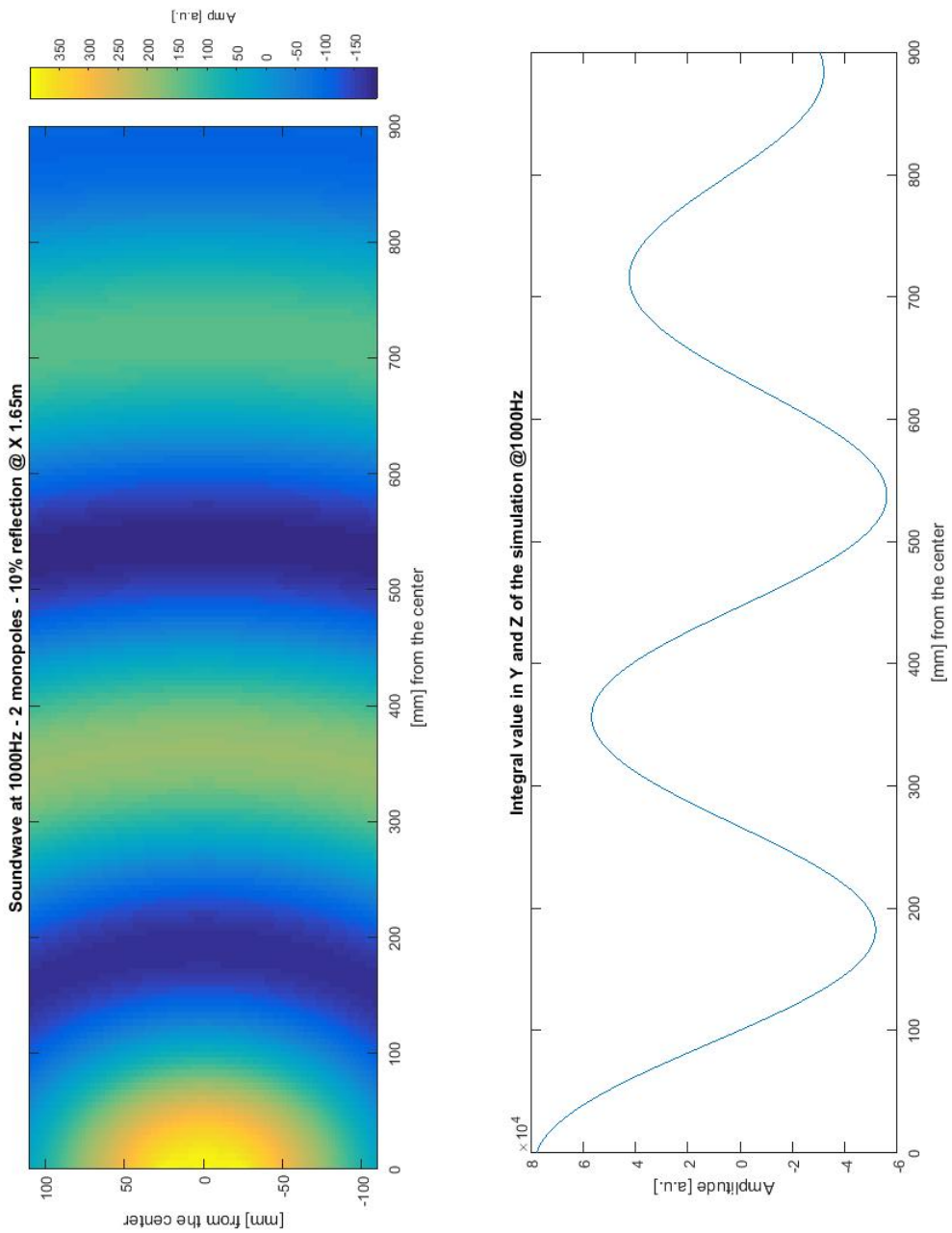

Figure 3.9: Simulated sound field at 1000 Hz, integral values in X-direction,integral values in X,Z-direction bottom

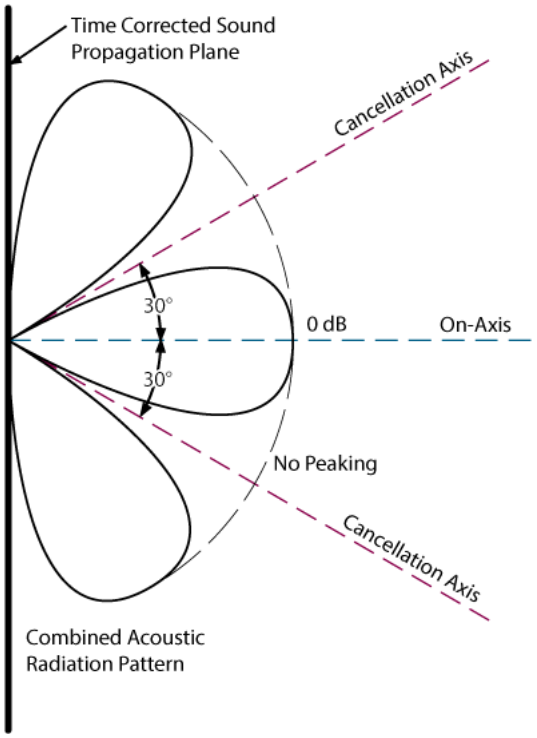

Figure 3.10: Directional characteristics of a speaker [49]

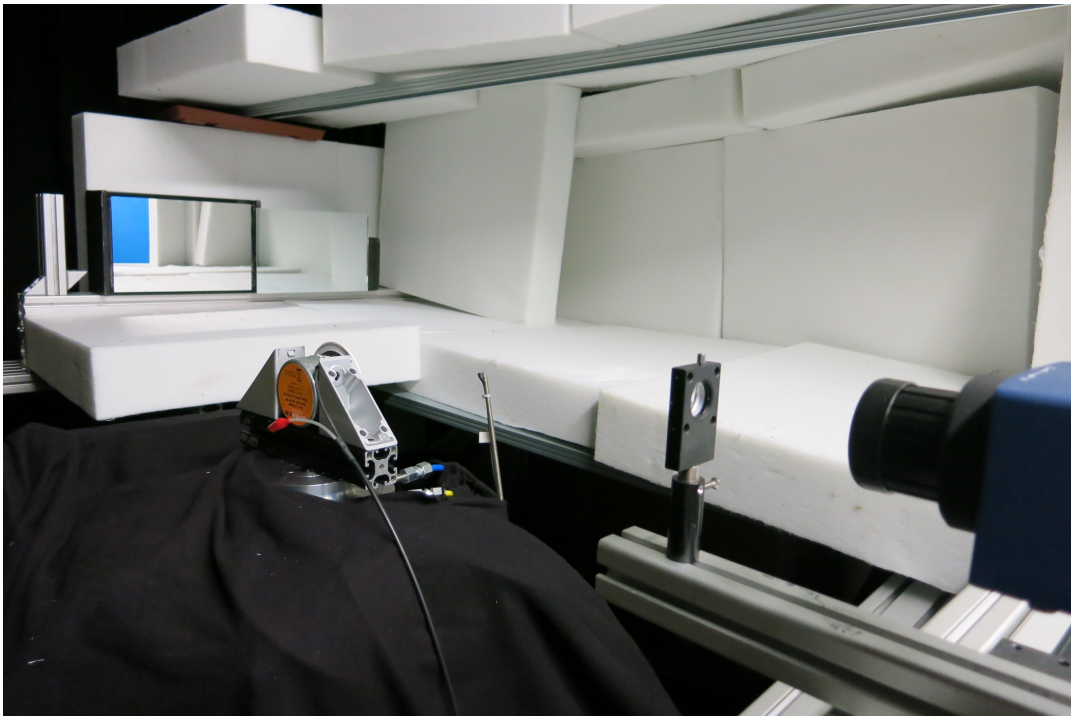

Figure 3.11: Setup with sound absorbing panels in tunnel shape (speaker in the center, LIV in foreground, mirror in background)

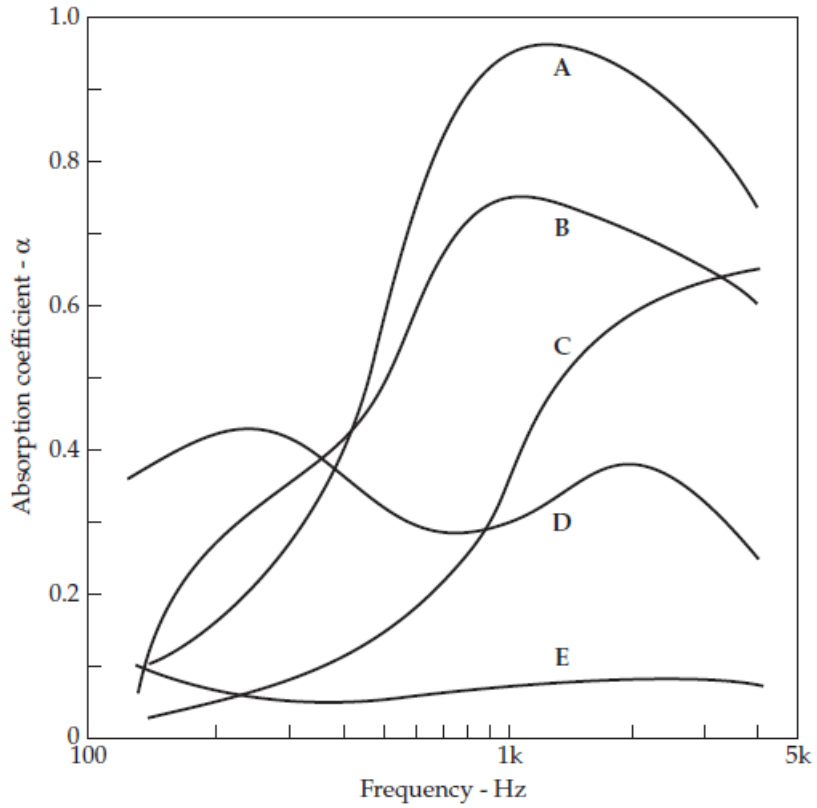

Figure 3.12: Sound absorption coefficients of typical porous materials A,B and C show a similarity in general shape. Good high frequency absorption and low frequency absorption characterize porous absorbers. (A) High-grade acoustic tile. (B) Medium weight ($0.47kg/m^2$) velour draped to half. (C) Heavy carpet on concrete without padding. (D) Coarse concrete blocks, unpainted. (E) Coarse concrete blocks, painted. [50]

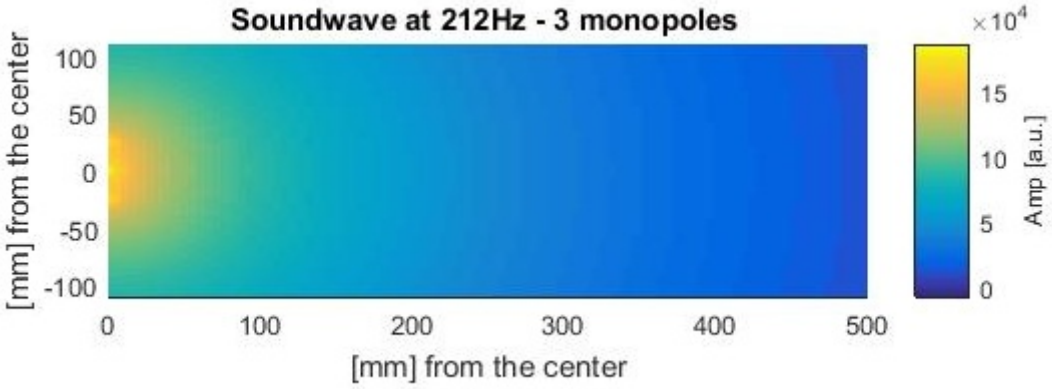

Figure 3.13: Simulated sound field at 212 Hz, three oscillating monopoles in phase were placed on the membrane of the speaker (spherical sound emission)

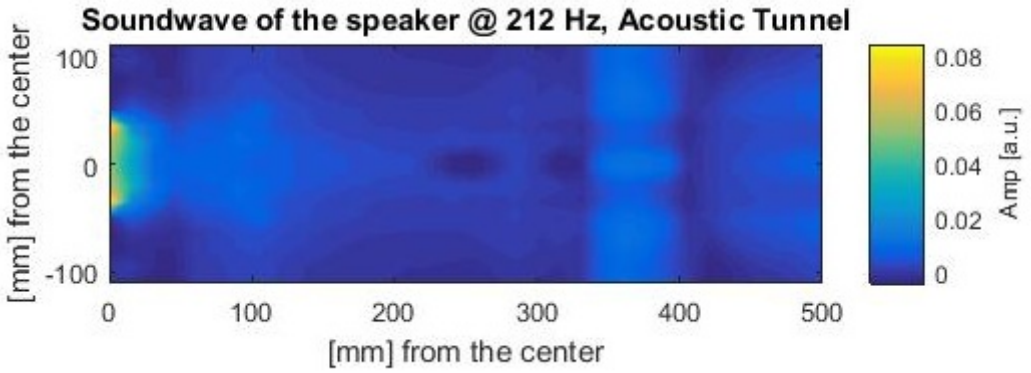

Figure 3.14: Sound field measured with the ISEL traversing unit. Acoustic absorbers arranged as tunnel

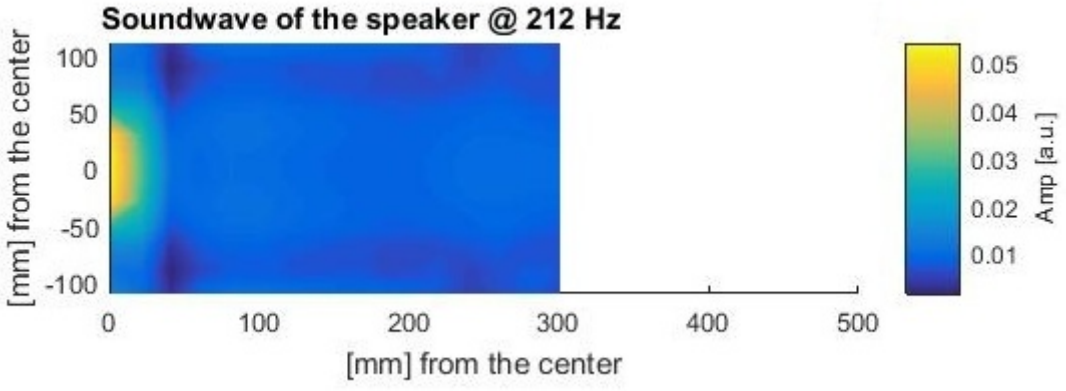

Figure 3.15: Sound field measured with the ISEL traversing unit. Acoustic absorbers arranged non-uniformly

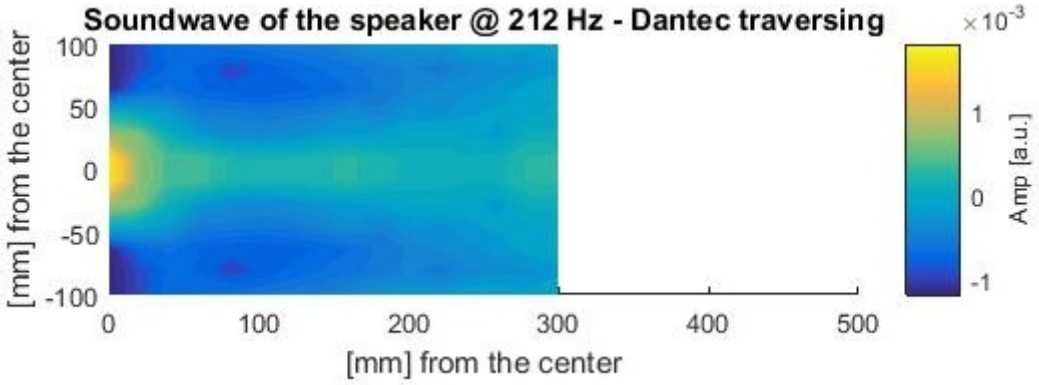

Figure 3.16: Using the Dantec traversing unit, removed ISEL traversing unit and mounts. (the speaker is traversed) acoustic absorbers arranged non-uniformly

3.3 Measurement of Acoustic Emissions of a Swirl Stabilized Methane Flame via LIV

From the previous recording using the loud-speaker we already know sources of error. (mainly reflections, see section 3.2) In this section a measurement on the flame at 212 Hz is discussed.

The acoustic absorber panels were partially removed from the cabinet, as this yielded the best results in previous measurements on the speaker. Due to the small traversing distance of $300mm \times 400mm$, the ISEL traversing unit was removed from the cabinet and the measurement was performed by traversing the burner on the Dantec traversing unit.

Before recording the acoustic field via LIV, a frequency resolved noise measurement of the flame was performed. This resulted in $67dB$ at a frequency of $\sim 212Hz$ at a distance of $0.5m$ of the flame. Taking in consideration the minimum detectable velocity of the LIV system which is $0.01\mu m/s$ and assuming a optical path of $0.1m$ at a distance of $0.5m$ where the acoustic wave is in phase along the $0.1m$ optical path and using the ideal gas equation and the relation for the OPL (see equation 2.1.2) we calculated a minimum detectable pressure amplitude of $0.03Pa$ or $60dB$, which represents a television on living-room level.

Further estimations were made after the measurement with the voltage signal from the LIV. This lead to an output voltage higher by a factor of 10 over the minimum detectable output voltage of the LIV. Thus, the error can be estimated within 10% of the output voltage.

Figure 3.17 shows the first measurement performed on the flame, with a consistently decreasing phase towards the right side of the plot. This measurement was conclusive for further acoustic measurements performed on the flame, because it proved the detectability of the acoustic emissions of the flame via LIV. The measurement time was $60s$, with an SL of $16384S$ and a SR of $16384S/s$. The measurement grid was chosen with $16 \times 20mm$ starting at $30mm$ for the Y-axis and $15 \times 20mm$ starting at $5mm$ for the Z-axis (similar as seen in figure 3.7).

A wider measurement grid was chosen to cover a bigger area surrounding the flame. The measurement grid was $16 \times 20mm$ in Y-axis and $21 \times 20mm$ in Z-axis. The measurement time was $60s$, with an SL of $10s$ and a SR of $16384S/s$. The real part of the CPSD can bee seen in figure 3.18. Due to the high-density fluctuation caused by the flame, the amplitude of the CPSD was reduced by the 5^{th} root for visualization. This will result in a decrease of the maximum amplitude and an amplification of smaller values.

In the top part, the convection zone (without reactions) above the flame can be observed. This was also observed in a measurement performed by F. Greiffenhagen as it can be seen in figure 3.19. Looking on the right side of figure 3.18 a steep decrease in the amplitude of the density fluctuations at a height of $150mm$ can also be observed in figure 3.19. This may be related to the non-uniform, chaotic, distribution of density fluctuations in the convection zone of the flame, which resembles white noise (see top left figure 3.19). Hence the noise emitted from the convective fluctuations cancels itself and no density fluctuations in the acoustic field can be observed.

Main sources of error (systematic errors influencing reliability and accuracy):

- Reflections of the sound waves from surrounding equipment (traverse, mirror, LIV mount etc.).
- Malfunction or not proper alignment of the equipment (e.g. laser beam collimation, please keep in mind: this measurement is close to the detection limit of a novel, digital LIV).

- When simulation results are compared to the data, different characteristics of the sound emission (other than spherical) have to be discussed.
- In understanding the sound field emitted by a flame, refraction of the sound waves by temperature fields and density gradients as well as sound reflection by the base plate must be taken into account.
- An change of operating point during operation of the burner (scanning time of the LIV) will lead to divergent phase information.

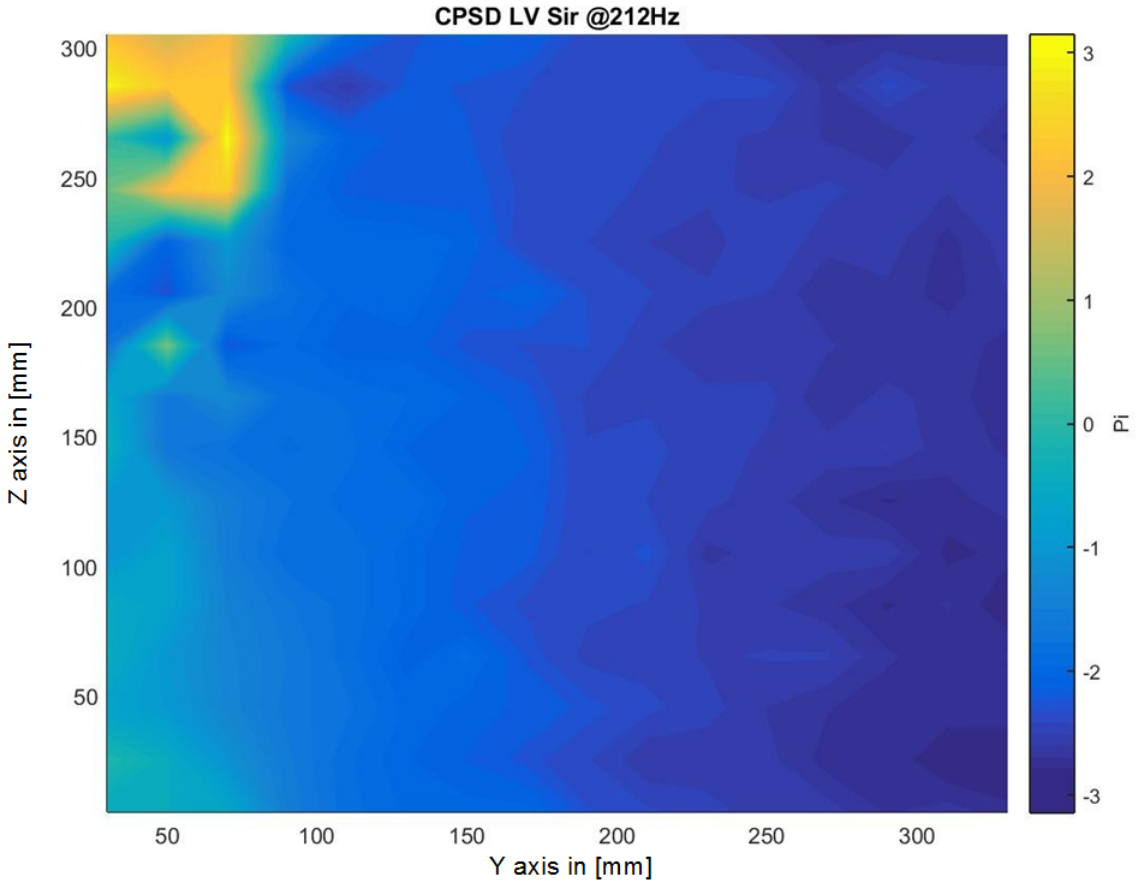

Figure 3.17: First LIV measurement of the flame, convective part (top left), sound emissions (right), no heat release (bottom left)

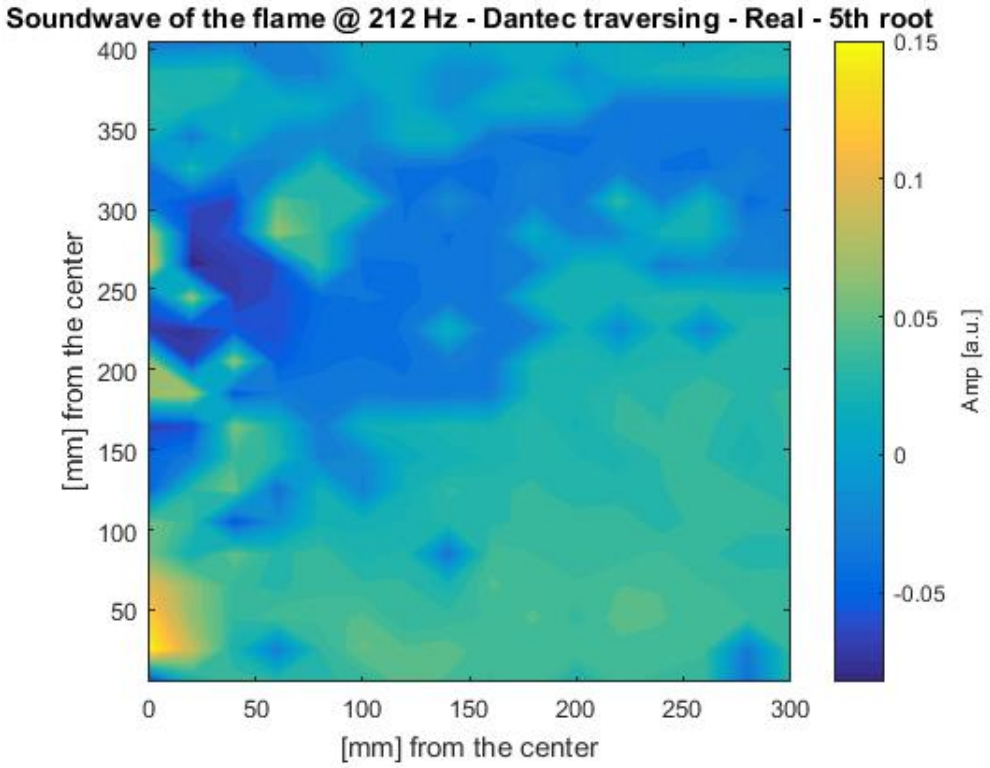

Figure 3.18: LIV measurement of Sound wave propagation (bottom right), convective part (top), flame (bottom left)

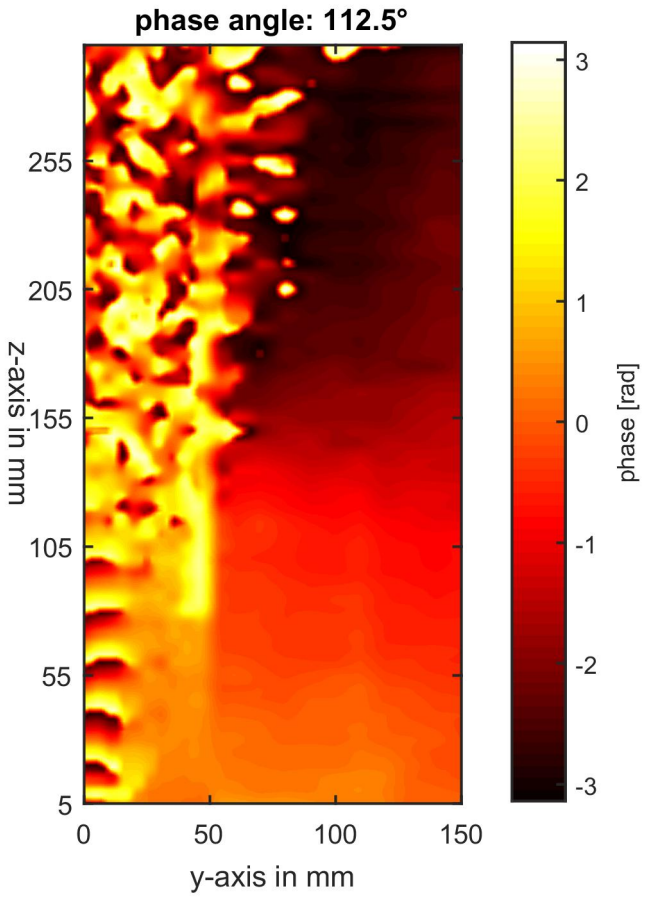

Figure 3.19: LIV measurement of the flame, convective part (top left), sound emissions (right), heat release (bottom left) [52]

4 Conclusion and Outlook

In the first part of this thesis, windowing for FFT-routines was investigated. The focus was set on the existing routines and the experiments performed in the area of laser-optical diagnostics and combustion & flames at the Institute of Thermal Turbomachinery and Machine Dynamics. Although windowing represents a powerful tool to improve the results obtained by any FFT routine, a longer sample rate resulting in $1/10Hz$ resolution with a uniform (rectangular) window was chosen. It was revealed that this setting yielded best and trustworthy results due to the single-frequency selection by the siren. Furthermore, the rotatory symmetry of the burner, which was first proven by Peterleithner [46], was observed again. Regarding Strahles theory [8], the density fluctuations in the flame recorded via LIV resulted in equal values of sound power as the values detected via the PP-probes, whenever above consideration about FFT transform are taken into account. In order to visualize the sound field emitted by the flame at $212Hz$, a first test (including simulation) was performed with a sound speaker.

The measurement of the $1000Hz$ sound field emitted by the sound speaker lead to very good results, where the simulation matches the measurement. This may be referred to the good damping characteristic of the curtains and absorber panels at such short wavelength.

Measuring the $212Hz$ signal of the speaker resulted in various deviations and problems, that could only be partially fixed. Due to the long wave length of $1.6m$ a measurement in the far field was not possible and therefore directional characteristics of the speaker have to be taken in account. Hence a simulation with oscillating monopoles will not perfectly fit the measurement.

The first measurement of the sound field flame at $212Hz$ did not yield a satisfactory result. Nevertheless, certain patterns observed in former measurements could be found in the acoustic field measurement. For an improvement of the experiment, acoustic absorbers with a high absorption coefficient at $212Hz$ were used. Additionally, according Sabine's equation (see equation 2.3.2), a bigger measurement cabinet might also enhance future results. Another opportunity would be the use of a different excitement frequency (closer to $1000Hz$) of the siren or the use of a more powerful burner for better signal-to-noise ratio. Regardless the above-mentioned optimized arrangements, a measurement at low frequency like 212 Hz will remain a difficult and challenging task for researcher and material.

The drawback of the LIV technique is its time demanding measuring procedure with the traversing in between each measurement point. Stability of siren and flame (CH_4 and air pressure lines) must be provided. Therefore a full-field laser vibrometer with an high speed camera sensor, as mentioned in section 3.3 or a scanning LIV will enhance the measurement process significantly. This also would take care of drifting points when operating the burner.

Conclusively, this thesis showcased the capability of the LIV to quantitatively detect locally resolved density fluctuations with precision and accuracy, resulting in the flow field in and around a flame, including zones of heat release and convection, as well as the sound fields emitted by the flame.

Bibliography

[1] A. Koopman, R. Ashok, and M. Bonnie, "The Gas Turbine Handbook." `https://www.netl.doe.gov/research/coal/energy-systems/turbines/publications/handbook`, 2006. [Accessed 16 10 2017].

[2] Y. Huang and V. Yang, "Dynamics and stability of lean-premixed swirl-stabilized combustion," *Progress in Energy and Combustion Science*, vol. 35, pp. 293–364, Aug. 2009.

[3] A. P. Dowling and Y. Mahmoudi, "Combustion noise," *Proceedings of the Combustion Institute*, vol. 35, pp. 65–100, Jan. 2015.

[4] ICAO, "Reduction of Noise at Source." `https://www.icao.int/environmental-protection/Pages/Reduction-of-Noise-at-Source.aspx`, 2017. [Accessed 16 10 2017].

[5] P. Gren, K. Tatar, J. Granström, N.-E. Molin, and E. V. Jansson, "Laser vibrometry measurements of vibration and sound fields of a bowed violin," *Measurement Science and Technology*, vol. 17, no. 4, p. 635, 2006.

[6] A. Harland, J. Petzing, and J. Tyrer, "Visualising scattering underwater acoustic fields using laser Doppler vibrometry," *Journal of Sound and Vibration*, vol. 305, pp. 659–671, Sept. 2007.

[7] L. Zipser, S. Lindner, and R. Behrendt, "Interferometrische Messung und Visualisierung von Schallwellen und Turbulenzen (Interferometric Measurement and Visualisation of Acoustic Waves and Vortexes)," *tm - Technisches Messen*, vol. 69, pp. 275–281, Sept. 2002.

[8] W. C. Strahle, "On combustion generated noise," *Journal of Fluid Mechanics*, vol. 49, pp. 399–414, 1971.

[9] T. J. B. Smith and J. K. Kilham, "Noise Generation by Open Turbulent Flames," *The Journal of the Acoustical Society of America*, vol. 35, pp. 715–724, May 1963.

[10] J. Peterleithner, S. Zerobin, and J. Woisetschläger, "Analysis of Combustion noise using locally resolved density fluctuations and a microphone array," *Proceedings of the ASME Turbo Expo, GT2016-57490*, 2016.

[11] T. Irvine, "Apollo 12 Pogo Oscillation." `http://www.vibrationdata.com/Newsletters/October2008_NL.pdf`, 2008. [Accessed 16 10 2017].

[12] J. J. Keller, "Thermoacoustic oscillations in combustion chambers of gas turbines," *AIAA Journal*, vol. 33, pp. 2280–2287, Dec. 1995.

[13] J. Hermann, C. Hantschk, P. Zangl, S. Gleis, D. Vortmeyer, J. Seume, N. Vortmeyer, W. Krause, and A. Orthmann, "Aktive Instabiltätskontrolle an einer 170 MW Gasturbine," *VDI-Bericht Nr. 1313*, 1997.

[14] C.-C. Chao and S. D. Heister, "Contributions of atomization to F-1 engine combustion instabilities," *Engineering Analysis with Boundary Elements*, vol. 28, pp. 1045–1053, Sept. 2004.

[15] S. R. Stow and A. P. Dowling, "Thermoacoustic Oscillations in an Annular Combustor," *ASME Turbo Expo 2001: Power for Land, Sea, and Air, 2001-GT-0037*, pp. –, June 2001.

[16] T. C. Lieuwen, "Experimental Investigation of Limit-Cycle Oscillations in an Unstable Gas Turbine Combustor," *Journal of Propulsion and Power*, vol. 18, pp. 61–67, Jan. 2002.

[17] F. A. Williams, *Combustion Theory: The Fundamental Theory of Chemically Reacting Flow Systems*. Combustion science and engineering series, Cambridge, Mass: Perseus Books, 2. ed., [nachdr.] ed., 2000.

[18] E. Hecht, *Optics*. Boston: Pearson Education Inc, 5 ed., 2017.

[19] R. G. Lyons, *Understanding Digital Signal Processing*. Upper Saddle River, NJ: Prentice Hall, 3 edition ed., Nov. 2010.

[20] A. V. Oppenheim and R. W. Schafer, *Digital Signal Processing*. Englewood Cliffs, N.J: Prentice-Hall, 1975.

[21] S. W. Smith, "The Scientist and Engineer's Guide to Digital Signal Processing." `http://www.dspguide.com/ch10.htm`, 2017. [Accessed 16 10 2017].

[22] F. J. Harris, "On the Use of Windows for Harmonic Analysis with the Discrete Fourier Transform," *Proceedings of the IEEE*, vol. 66, pp. 51–83, 1978.

[23] S. Scholl, "Exact Signal Measurements using FFT Analysis." `https://kluedo.ub.uni-kl.de/files/4293/exact_fft_measurements.pdf`, 2016. [Accessed 19 10 2017].

[24] J. Woisetschläger, N. Mayrhofer, H. Lang, and B. Hampel, "Experimental Investigation of Turbine Wake Flow by Interferometrically Triggered PIV and LDV Measurements," pp. 207–216, ASME, 2000.

[25] N. Mayrhofer and J. Woisetschläger, "Frequency analysis of turbulent compressible flows by laser vibrometry," *Experiments in Fluids*, vol. 31, pp. 153–161, Aug. 2001.

[26] B. Hampel and J. Woisetschläger, "Frequency- and space-resolved measurement of local density fluctuations in air by laser vibrometry," *Measurement Science and Technology*, vol. 17, no. 10, p. 2835, 2006.

[27] F. Giuliani, B. Wagner, J. Woisetschläger, and F. Heitmeir, "Laser Vibrometry for Real-Time Combustion Stability Diagnostic," vol. 2006, pp. 603–610, ASME, 2006.

[28] S. Köberl, F. Fontaneto, F. Giuliani, and J. Woisetschläger, "Frequency-resolved interferometric measurement of local density fluctuations for turbulent combustion analysis," *Measurement Science and Technology*, vol. 21, no. 3, p. 035302, 2010.

[29] T. Leitgeb, T. Schuller, D. Durox, F. Giuliani, S. Köberl, and J. Woisetschläger, "Interferometric determination of heat release rate in a pulsated flame," *Combustion and Flame*, vol. 160, pp. 589–600, Mar. 2013.

[30] T. Leitgeb, *On the Design and Validation of a Variable Geometry Burner Concept*. PhD thesis, TU Graz, Graz, 2012.

[31] F. Giuliani, J. Woisetschläger, and T. Leitgeb, "Design and validation of a burner with variable geometry for extended combustion range," *ASME Turbo Expo 2012: Turbine Technical Conference and Exposition, GT2012-68236*, pp. 155–165, 2012.

[32] J. Peterleithner, A. Marn, and J. Woisetschläger, "Interferometric Investigation of the Thermoacoustics in a Swirl Stabilized Methane Flame," *ASME Turbo Expo 2015: Turbine Technical Conference and Exposition, GT2015-42743*, pp. –, June 2015.

[33] J. Peterleithner, R. Basso, F. Heitmeir, J. Woisetschläger, R. Schlüßler, J. Czarske, and A. Fischer, "Comparison of Flame Transfer Functions Acquired by Chemiluminescence and Density Fluctuation," *ASME Turbo Expo 2016: Turbomachinery Technical Conference and Exposition, GT2016-57485*, pp. –, June 2016.

[34] F. Greiffenhagen, J. Peterleithner, and J. Woisetschläger, "Prediciton of combustion noise of a swirl stabiled flame using laser interferometric vibrometry validated by acoustic measurements," *Proceedings of the ASME Turbo Expo, GT2017-63418*, 2017.

[35] J. Dongarra and F. Sullivan, "Guest Editors Introduction to the top 10 algorithms," *Computing in Science Engineering*, vol. 2, pp. 22–23, Jan. 2000.

[36] E. O. Brigham, *The Fast Fourier Transform and Its Applications*. Prentice-Hall signal processing series, Englewood Cliffs, N.J: Prentice Hall, 1988.

[37] J. B. J. baron Fourier, *Théorie analytique de la chaleur*. Chez Firmin Didot, père et fils, 1822.

[38] G. Walz, *Lexikon der Mathematik. Bd.2: Eig bis Inn*. Berlin, Heidelberg: Springer Berlin Heidelberg, 2 ed., 2017.

[39] E. Kreyszig, *Advanced Engineering Mathematics*. Hoboken, NJ: John Wiley & Sons Inc, 10 ed., Dec. 2010.

[40] J. W. Cooley and J. W. Tukey, "An Algorithm for the Machine Calculation of Complex Fourier Series," *Mathematics of Computation*, vol. 19, no. 90, pp. 297–301, 1965.

[41] H. Süße and E. Rodner, *Bildverarbeitung und Objekterkennung: Computer Vision in Industrie und Medizin*. Wiesbaden: Springer Vieweg, 1 ed., Sept. 2014.

[42] C. E. Shannon, "Communication in the Presence of Noise," *Proceedings of the IRE*, vol. 37, pp. 10–21, Jan. 1949.

[43] James Cole, "Rolling Shutters." `https://jasmcole.com/2014/10/12/rolling-shutters/`, 2014. [Accessed 16 10 2017].

[44] Matlab, "Welch's power spectral density estimate - MATLAB pwelch - MathWorks Deutschland." `https://de.mathworks.com/help/signal/ref/pwelch.html`, 2017. [Accesseed 16 10 2017].

[45] NI, "Understanding FFTs and Windowing.pdf." `http://download.ni.com/evaluation/pxi/Understanding%20FFTs%20and%20Windowing.pdf`, 2017. [Accessed 16 10 2017].

[46] J. Peterleithner, J. Woisetschläger, and T. Leitgeb, "Frequency resolved interferometrics detection of local density fluctuations in flames," *Proc. 17th Symposium on Application of Laser Techniques to Fluid Mechanics, Lisbon, paper 04.7_1_53*, 2014.

[47] F. Giuliani, A. Lang, K. Johannes Gradl, P. Siebenhofer, and J. Fritzer, "Air Flow Modulation for Refined Control of the Combustion Dynamics Using a Novel Actuator," *Journal of Engineering for Gas Turbines and Power*, vol. 134, no. 2, p. 021602, 2012.

[48] J. Peterleithner, N. V. Stadlmair, J. Woisetschläger, and T. Sattelmayer, "Analysis of Measured Flame Transfer Functions With Locally Resolved Density Fluctuation and OH-Chemiluminescence Data," *Journal of Engineering for Gas Turbines and Power*, vol. 138, p. 031504, Sept. 2015.

[49] RANE, "Linkwitz-Riley Crossovers: A Primer." `http://www.rane.com/note160.html`, 2005. [Accessed 16 10 2017].

[50] F. A. Everest and K. Pohlmann, *Master Handbook of Acoustics*. New York: McGraw-Hill/TAB Electronics, 5 edition ed., June 2009.

[51] Author not named, *Sound Intensity*. Brüel&Kjaer, 1993.

[52] F. Greiffenhagen, J. Peterleithner, Gürtler, A. Fischer, J. Woisetschläger, and J. Czarske, "Quantitative measurement and estimation of uncertainties of density fluctuations in swirl stabilized flames with laser interferometric vibrometry." [for publication], Oct. 2017.

Appendix

A.1 Appendix 1

Derivation of equation 2.1.8 from section 2.1.

For the isentropic pressure derivative ideal gas with $p = \rho RT$, $\boldsymbol{T}$ the ***temperature***, $\boldsymbol{R}$ the ***gas constant***, the relation $pv^{\kappa} = const.$, with $\boldsymbol{\kappa}$ as the ***ratio of the heat capacities*** and $\boldsymbol{v}$ the ***specific volume*** $\boldsymbol{\rho^{-1}}$ are assumed and lead to equation A.1.1.

$$\frac{\partial \rho(s,p)}{\partial p}\Big|_s = \frac{v^{\kappa}}{\kappa p v^{\kappa+1}} = \frac{1}{\kappa RT} = \frac{1}{c^2} \tag{A.1.1}$$

With ***c the local speed of sound***.

With the second law of thermodynamics, (***reversible heat*** q), the entropy can be written as followed:

$$Tds = dq \tag{A.1.2}$$

For q:

$$dq = du + p\ dv \tag{A.1.3}$$

For the ***enthalpy h***:

$$dh = du + p\ dv + v\ dp \tag{A.1.4}$$

Where the second term right hand side can be discarded, since we are assuming isobar conditions.

Hence:

$$Tds = dq = du + p\ dv = dh \tag{A.1.5}$$

Expressing the enthalpy with the ***heat ratio at constant pressure*** $\boldsymbol{c_p}$, T and the ideal gas law we get:

$$ds = \frac{dh}{T} = c_p \frac{dT}{T} = c_p\ d(\frac{p}{\rho RT}) = -\frac{c_p\ p}{R\rho^2 T}\ d\rho = -\frac{c_p}{\rho}\ d\rho \tag{A.1.6}$$

Integration and partial derivation of equation A.1.6 leads to:

$$\frac{\partial \rho}{\partial s} = -\frac{R\rho^2}{c_p\ pT} = -\frac{\rho}{c_p} \tag{A.1.7}$$

With the results from equation A.1.7 and equation A.1.1 equation 2.1.7 derived by time results in:

$$\frac{d\rho(s,p)}{dt} = \frac{1}{c^2}\frac{dp}{dt} - \frac{\rho}{c_p}\frac{ds}{dt} = \frac{1}{c^2}\frac{dp}{dt} - \frac{\rho}{c_p\,T}\frac{dq}{dt} = \frac{1}{c^2}\frac{dp}{dt} - \frac{\kappa-1}{c^2}\frac{dq_v}{dt} \tag{A.1.8}$$

A.2 Appendix 2

Appendix to the relation between density fluctuations and heat release rate. The following text is taken from a manuscript submitted to Combustion & Flame in 2017. The contributors of the manuscript are Greiffenhagen, Peterleithner, Gürtler, Fischer, Woisetschläger and Czarske. The manuscript will be published in a paper in the near future.

"Within the flame a more detailed transport equation (Williams' equation) is needed to discuss all effects in a reactive gas. Such a discussion can be found in a number of references [A1, A2, A3] and is summarized here, as far as it is important for a correct interpretation of the measurements. Williams' equation includes N species with mass fractions Y_k and enthalpies h_k , index $n = 1 \dots N$, the heat flux vector Q, flow velocities u_i, and the viscous stress tensor $\tau_i j$.

$$\frac{d\rho}{dt} = \frac{1}{c^2}\frac{dp}{dt} + \frac{\kappa-1}{c^2}\Big\{\sum_{n=1}^{N}\frac{\partial h}{\partial Y_n}\Big|_{\rho,p,Y_m}\rho\frac{dY_n}{dt} + \nabla.Q - \tau_i j\frac{\partial u_i}{\partial x_j}\Big\} \tag{A.2.1}$$

The expression Y_m with $m \neq n$ means that all other molecular contributions are frozen during summation. While the pressure term is identical to the one in eq. A.1.8, the heat term includes the heat addition from the chemical reaction, the heat flux and the heat input from friction. The first term in the bracket is transformed using the chain rule

$$\frac{\partial h}{\partial Y_n}\Big|_{T,p,Y_m} = \frac{\partial h}{\partial Y_n}\Big|_{\rho,p,Y_m} + \frac{\partial h}{\partial \rho}\Big|_{p,Y_m}\frac{\partial \rho}{\partial Y_n}\Big|_{T,p,Y_m} \tag{A.2.2}$$

The right term in eq. A.2.2 is the change in density at constant T and p and is caused by changes in species concentrations. Burning hydrocarbons in air, the changes in mixture molar mass remain weak, the average molecular weight is constant, so this term equals zero. Using the conservation of species

$$\rho\frac{dY_n}{dt} = \frac{d\omega_n}{dt} - \nabla J_n \tag{A.2.3}$$

with $d\omega_n/dt$ the production rate of species n and Jn the flux of species n by diffusion, and neglecting later since the contribution by species diffusion is small compared to the production rate in the flame, eq. A.2.3 simplifies to

$$\rho\frac{d\rho}{dt} = \frac{1}{c^2}\frac{dp}{dt} - \frac{\kappa-1}{c^2}\Big\{\frac{dq_v}{dt} + \tau_i j\frac{\partial u_i}{\partial x_j} - \nabla.Q\Big\} \tag{A.2.4}$$

with q_v the volumetric heat released by combustion. The term in the bracket includes the heat input by combustion, the input from friction and the losses by radiation or conduction to the walls. When heat released by friction is small compared to the heat released by the combustion, and neglecting thermal radiation from CO2 and H2O (lean combustion) one gets

$$\frac{d\rho}{dt} = \frac{1}{c^2}\frac{dp}{dt} - \frac{\kappa - 1}{c^2}\left\{\frac{dq_v}{dt} + \nabla.(\lambda \nabla T)\right\} \tag{A.2.5}$$

with λ the thermal conductivity. This loss term is important when close to the combustion chamber wall. For an unconfined flame eq. A.2.5 equals eq. A.1.8 and eq. 2.1.8 for the heat release fluctuations.

In isothermal flows, the heat input is zero and the density fluctuations represent the pressure fluctuations in the system

$$\frac{d\rho'}{dt} = \frac{1}{c^2}\frac{dp'}{dt} \tag{A.2.6}$$

Using eq. A.2.6 LIV can be applied for turbulence research [A4, A5, A6], for the detection of acoustic fields around machines [A6] or music instruments [A8], and for underwater acoustics [A9]. When heat is added to the flow by combustion the order of magnitude for the single contributions to eq A.2.5 can be estimated by

$$\rho' = \frac{1}{c^2}p' - \frac{\kappa - 1}{c^2}q'_v \tag{A.2.7}$$

With $\bar{\rho} \cong 1\breve{}0.5kg/m^3$, $\rho'/\rho \hat{=} 0.2\breve{}0.5$, $c = 500m/s$, and $p' = 1000Pa$, the pressure fluctuations are 2 orders of magnitude smaller than the fluctuations in density, therefore

$$\frac{\partial \rho'}{\partial t} = -\frac{\kappa - 1}{c^2}\frac{\partial q'_v}{\partial t} \tag{A.2.8}$$

is valid for the combustion zone, but only if the frequencies of the fluctuations are not close to the thermo-acoustic resonance frequency of the combustion chamber. Starting without pressure fluctuations, substituting the speed of sound $c^2 = \kappa RT$, and using the relation for a perfect gas $p = \rho RT$, eq.A.2.8 changes to

$$\frac{1}{\rho}\frac{d\rho'}{dt} = -\frac{\kappa - 1}{p\kappa}\frac{dq'_v}{dt} \tag{A.2.9}$$

This step substitutes the temperature by density. With fluctuations (ρ') and steady state ($\bar{\rho}$) variables we obtain

$$\frac{1}{\bar{\rho} + \rho'}\frac{d\rho'}{dt} = -\frac{\kappa - 1}{p\kappa}\frac{dq'_v}{dt} \tag{A.2.10}$$

While LIV is capable to record density fluctuations with high accuracy and precision, it is necessary to use another optical technique such as shearography or background-oriented schlieren to detect absolute density quantitatively.

Beside detailed information about heat release in the flame, the density fluctuations also provide information about the acoustic far field of the flame. Pressure fluctuations in the far field of a turbulent swirl-stabilized flame can be calculated directly if density fluctuations in the flame are known as a function of time and space [A10, A11]. [A12]"

[*A*1] Candel S., Durox D., Schuller T., Bourgoin J.-F., Moeck J.P., Dynamics of Swirling Flames, *Annual Review of Fluid Mechanics,* vol. 46, pp. 147-173, 2014

[*A*2] Crighton D.G., Dowling A.P., Ffowcs W. J.E., Heckl M., Leppington F.G., Modern Methods in Analytical Acoustics, *Springer Verlag Berlin Heidelberg,* 1992

[*A*3] Williams F.A., Combustion Theory, *Perseues Books,* 1985

[*A*4] Woisetschläger J., Mayrhofer N., Hampel B., Lang H. and Sanz W., "Laser-optical investigation of turbine wake flow", *Experiments in Fluids,* vol. 34, pp. 371-378, 2003

[*A*5] Martarelli M., Castellini P., Tomasini E.P., "Subsonic jet pressure fluctuataion characterization by tomographic laser interferometry", *Experiments in Fluids,* vol. 58, pp. -, 2013

[*A*6] Mayrhofer N., Woisetschläger J., "Frequency analysis of turbulent compressible flows by laser vibrometery", *Eyperiments in Flames,* vol. 31, pp. 153-161, 2001

[*A*7] Zipser L., Lindner S., Behrendt R., "Interferometrische Messung und Visualisierung von Schallwellen und Turbulenzen", *Teschnisches Messen,* vol. 69, pp. 275-281, 2002

[*A*8] Gren P., Tatar K., Granström J., Molin N.-E., Jansson E. V., "Laser vibrometry measurements of vibration and sound fields of a bowed violin", *Measurement Science and Technology,* vol. 17, pp. 635, 2006

[*A*9] Harland A.R., Petzing J.N., Tyrer J.R., "Visualising scattering underwater acoustic fields using laser Doppler vibrometry", vol. 305, pp. 659-671, *Journal of Sound and Vibration,* 2007

[*A*10] Strahle W.C., "Some results in combustion generated noise", *Journal of Sound and Vibration,* vol. 49, pp. 399-414, 1972

[*A*11] Greiffenhagen F.,Peterleithner J.,Woisetschläger J., "Prediction of combustion noise of a Swirl-stabilized flame using laser interferometric vibrometry validated by Acoustic measurements", *Proceedings ASME Turbo Expo, GT2017-63418,* 2017

[*A*12] Greiffenhagen F., Peterleithner J., Gürtler, Fischer A., Woisetschläger J., Czarske J., "Quantitative measurement and estimation of uncertainties of density fluctuations in swirl stabilized flames with laser interferometric vibrometry", [for publication], 2017

A.3 Appendix 3

The following code represents a Matlab routine for a single time signal calculating the PSD and the RMS values in frequency doain.

```
%************************************************************************
%Funktion liest Zeitsignale mit Endung '*.txt' ein und fuehrt danach FFT,
%berechnet das Leistungsspektrum und speichert anschliessend sowohl das
%Ergebnis der FFT als auch das Powerspektrum in eigenen Dateien mit der
%Endung '*.dat' ab
%************************************************************************

%************************************************************************
% edit: Wiesinger 06.2017
% - now uses PWELCH and FFT.
```

```
11      % - will truncate Samples that do not fill up for a multiple integer of the Sample ...
            Rate (Sample_size =
12      % n*Sample_Rate)
13
14      function fft_jakob_SL_corr
15
16
17      %Eingabefenster fuer die Sampelrate und die Sampellaenge wird erstellt und
18      %Werte werden eingelesen.
19
20       prompt = {'Samplerate [Samplewerte/s]:','Sampellaenge [Anzahl ...
             Stuetzstellen]:','Window-Function: 0= Rect., 1= Flattop., 2= Hamming' };
21       dlg_title = 'Eingabe Daten fuer FFT';
22       num_lines = 1;
23       def = {'4096','4096','0'};
24       options.Resize='on';
25       options.WindowStyle='normal';
26       answer = inputdlg(prompt,dlg_title,num_lines,def,options);
27
28      % 01.06.2017 Umgeaendert auf PWELCH - Wiesinger
29      SR  = str2num(answer{1}); %uebergabe der Samplerate aus der Alten Routine an PWELCH ...
            variable
30      SL= str2num(answer{2}); %Sampel length
31
32      switch str2num(answer{3}) %% Berechnen des FFT windows.
33          case 0
34              win = ones(SL,1);%Rectangular window
35          case 1
36              win = flattopwin(SL); %flattop window
37          case 2
38              win = hann(SL); % hanning window
39          otherwise
40          error('Error: Window parameter does not match demanded value. Restart');
41      end
42
43
44      %Ordner, in dem die Zeitsignal-files liegen auswaehlen ordnerinhalt liest
45      %alle files mit der Endung '*.txt' ein, Ordner zum abspeichern der
46      %FFT-transformierten files und der Powerspektrums files werden angelegt
47
48
49       [fnamen, fpfad]=ordnerinhalt(3,'*.txt'); %einlesen des ordners
50       mkdir([fpfad '\FFT']); % anlegen des ordners "FFT"
51       mkdir([fpfad '\PSpectra']); %anlegen des ordners "PSpectra"
52
53       id=0;
54       nend=length(fnamen);
55
56       Δ_f=str2num(answer{1})/(2*(str2num(answer{2})/2)); %einlesen der antwort
57       frequenz=[0:(str2num(answer{2})/2)-1]'; %einlesen der antwort
58       frequenz=frequenz.*Δ_f; %berechnen des frequenz vektors
59
60
61
62       %waitbar wird aufgerufen
63
64       h=waitbar(0,'Berechnungsfortschritt FFT');
65
66       while id<nend
67
68           %files werden geladen. Sobald file geladen erscheint 'loaded'
69
70
71
72          id=id+1;
```

```
73          name=[fpfad '\' fnamen{id}];
74          time=tloadStef(name);
75          col=floor(numel(time)/SR); % Anzal der elemente die in ein Sample passen. Rest ...
                wird verschmissen.
76          time=time(1:col*SR);
77
78          disp('Loaded.')
79          %Zeitsignale werden in fftavCplxStef in Samples gleicher Laenge
80          %unterteilt und anschliessend foueriertransformiert und in Matrix
81          %zurueckgegeben
82
83          Ss1 = pwelch(time,win,0,SL,SR);% Calculating PSD
84          S1 = sum(win); % Calculating ENBW
85          S2 = sum(win.^2); % Calculating ENBW
86          NENBW = length(win)*S2/(S1^2); % Calculating ENBW
87          ENBW = (SR/SL)*NENBW; % Calculating ENBW
88          Ss1=Ss1*ENBW; % Correction of PSD with Equivalent Noise Band With --> PS = PSD*ENBW
89          Ss1=Ss1(1:end-1); % Truncating nyquist bin
90          Ss2=sqrt(Ss1); % Calculating RMS value
91
92          clear time;
93
94          OutSpec=[frequenz,Ss1]; % Erstellen des neuen Arrays fuer export
95          OutSpec1=[frequenz,Ss2]; %  Erstellen des neuen Arrays fuer export
96
97          %Festlegen des Pfads unter dem die Dateien abgespeichert werden und
98          %abspeichern
99
100         namebase=[fpfad '\FFT\fft_RMS_' fnamen{id}];
101         namebase1=[fpfad '\PSpectra\ps_' fnamen{id}];
102
103         dlmwrite(namebase1,OutSpec,'\t');
104         dlmwrite(namebase,OutSpec1,'\t');
105
106         waitbar(id/nend,h);
107      end
108      close(h);
109      dlmwrite([fpfad '\FFT\frequenzaufloesung.txt'],Δ_f,'\t'); %speichern
110      dlmwrite([fpfad '\PSpectra\frequenzaufloesung.txt'],Δ_f,'\t');
111      disp('Finished.')
112   end
```

A.4 Appendix 4

The following code represents a Matlab routine for two time signals calculating the CPSD, PSD and the RMS values in frequency domain.

```
1   %************************************************************************
2   %Funktion liest Zeitsignale mit Endung '*.txt' ein und fuehrt danach FFT,
3   %berechnet das Leistungsspektrum und speichert anschliessend sowohl das
4   %Ergebnis der FFT als auch das Powerspektrum in eigenen Dateien mit der
5   %Endung '*.dat' ab
6   %************************************************************************
7   %Edit Wiesinger 06.2017: CPSD berechnet ueber funktion PWELCH.
8   %
9
10  function fft_jakob_SL_corr
11
12
```

```
13      %Eingabefenster fuer die Sampelrate und die Sampellaenge wird erstellt und
14      %Werte werden eingelesen.
15
16        prompt = {'Samplerate [Samplewerte/s]:','Sampellaenge [Anzahl ...
              Stuetzstellen]:','Window-Function: 0= Rect., 1= Flattop., 2= Hamming' };
17       dlg_title = 'Eingabe Daten fuer FFT';
18       num_lines = 1;
19       def = {'16384','16384','0','0'};
20       options.Resize='on';
21       options.WindowStyle='normal';
22       answer = inputdlg(prompt,dlg_title,num_lines,def,options);
23
24       % 01.06.2017 Umgeaendert auf PWELCH
25      SR  = str2num(answer{1}); %uebergabe der Samplerate aus der Alten Routine an PWELCH ...
            variable
26      SL= str2num(answer{2}); %Sampel laenge
27      noverlap=0; %overlap
28
29      switch str2num(answer{3}) %% Berechnen der FFT windows.
30          case 0
31              win = ones(SL,1); %rectangular window
32          case 1
33              win = flattopwin(SL); %flattop window
34          case 2
35              win = hann(SL); %hanning window
36          otherwise
37          error('Error: Window parameter does not match demanded value. Restart');
38      end
39
40      %Ordner, in dem die Zeitsignal-files liegen auswaehlen ordnerinhalt liest
41      %alle files mit der Endung '*.txt' ein, Ordner zum abspeichern der
42      %FFT-transformierten files und der Powerspektrums files werden angelegt
43
44
45       [fnamen, fpfad]=ordnerinhalt(3,'*.txt'); %durchsucht ordnerinhalt nach *.txt
46       mkdir([fpfad '\FFT1']); %erstellt ordner
47       mkdir([fpfad '\PSpectra1']); %erstellt ordner
48       mkdir([fpfad '\FFT2']); %erstellt ordner
49       mkdir([fpfad '\PSpectra2']); %erstellt ordner
50       mkdir([fpfad '\Cross-spectra']); %erstellt ordner
51
52       id=0;
53       nend=length(fnamen);
54
55       Δ_f=str2num(answer{1})/(2*(str2num(answer{2})/2)); %einlesen der antwort
56       frequenz=[0:(str2num(answer{2})/2)-1]'; %einlesen der antwort
57       frequenz=frequenz.*Δ_f; %berechnen des frequenz vektors
58
59
60       %waitbar wird aufgerufen
61
62       h=waitbar(0,'Berechnungsfortschritt FFT');
63
64       while id<nend
65
66           %files werden geladen. Sobald file geladen erscheint 'loaded'
67
68          id=id+1;
69          name=[fpfad '\' fnamen{id}];
70          time=tloadStef(name);
71          disp('Loaded.')
72
73          [a,b]=size(time);
74
75          if a>b % Drehen falls 90 grad gekippt
```

```
76              time=time';
77              [a,b]=size(time);
78          end
79
80          %Falls zwei Zeitsignale aufgenommen, wird auch 2-tes Signal ausgewertet
81          if a>1
82
83              %Leistungsspektrum wird berechnet, danach werden
84              %Anteile ueber Nyquistfrequenz abgeschnitten
85
86              Power_Spec = pwelch(time(2,:),win,noverlap,SL,SR); % Power_spec for Power ...
                    spectral density
87
88              S1 = sum(win); % Calculating NENBW
89              S2 = sum(win.^2); % Calculating NENBW
90              NENBW = length(win)*S2/(S1^2); % Calculating NENBW
91              ENBW = (SR/SL)*NENBW; % Calculating ENBW
92
93
94
95              Power_Spec=Power_Spec(1:end-1)*ENBW; %cutting away nyquist bin and ...
                    Correcting it with ENBW
96              OutSpec22=[frequenz,Power_Spec];
97
98
99              %Berechnung der Amplitude und der Phase fuer fourietransformiertes
100             %Spektrum und anschliessende Mittelung ueber Anzahl der Spektren
101
102             FFT_Amp=sqrt(Power_Spec); %Berechnung des RMS wertes
103             OutSpec2=[frequenz,FFT_Amp]; %Erstellen der Frequenz-RMS-Matrix
104
105             %Berechnung des Kreuzspektrums zwischen Spektren von Zeitsignal 1
106             %und Zeitsignal 2, Ausgabe in Amplitude und Phase
107
108             Cross=cpsd(time(1,:),time(2,:),win,noverlap,SL,SR); % Berechnung CPSD
109             Cross=Cross(1:end-1); % verwerfen von nyquist
110             Amp=abs(Cross); %Berechnung der amplitude
111             Ang=angle(Cross); %Berechnung der Phase Angle
112             OutSpec21=[frequenz,Amp,Ang]; % Erstelleb der Frequenz-Amplitude-Winkel-Matrix
113
114             %ordnernamen werden vergeben.
115             namebase2=[fpfad '\FFT2\fft_2_RMS_' fnamen{id}];
116             namebase22=[fpfad '\PSpectra2\ps_2_' fnamen{id}];
117             namebase21=[fpfad '\Cross-spectra\Cs_' fnamen{id}];
118
119             dlmwrite(namebase2,OutSpec2,'\t'); %speichern
120             dlmwrite(namebase22,OutSpec22,'\t'); %speichern
121             dlmwrite(namebase21,OutSpec21,'\t'); %speichern
122         end
123
124
125         %Leistungsspektrum wird berechnet, danach werden
126         %Anteile ueber Nyquistfrequenz einfach abgeschnitten
127
128         S1 = sum(win); % Calculating ENBW
129         S2 = sum(win.^2); % Calculating ENBW
130         NENBW = length(win)*S2/(S1^2); % Calculating ENBW
131         ENBW = (SR/SL)*NENBW; % Calculating ENBW
132
133         Power_Spec_2 = pwelch(time(1,:),win,noverlap,SL,SR)*ENBW; % Power_spec for ...
                Power spectral
134         Power_Spec_2 = Power_Spec_2(1:end-1); %cutting away nyquist bin
135         OutSpec11=[frequenz, Power_Spec_2 ];
136
137
```

```
138          %Berechnung der Amplitude FFT
139          FFT_Amp_2=sqrt(Power_Spec);
140          OutSpec1=[frequenz,FFT_Amp_2];
141
142          %Festlegen des Pfads unter dem die Dateien abgespeichert werden und
143          %abspeichern
144
145          namebase1=[fpfad '\FFT1\fft_1_RMS_' fnamen{id}];
146          namebase11=[fpfad '\PSpectra1\ps_1_' fnamen{id}];
147
148         dlmwrite(namebase11,OutSpec11,'\t');
149         dlmwrite(namebase1,OutSpec1,'\t');
150          clear time;
151          waitbar(id/nend,h);
152       end
153       close(h);
154       dlmwrite([fpfad '\FFT1\frequenzaufloesung.txt'],Δ_f,'\t');
155       dlmwrite([fpfad '\PSpectra1\frequenzaufloesung.txt'],Δ_f,'\t');
156       dlmwrite([fpfad '\FFT2\frequenzaufloesung.txt'],Δ_f,'\t');
157       dlmwrite([fpfad '\PSpectra2\frequenzaufloesung.txt'],Δ_f,'\t');
158       dlmwrite([fpfad '\Cross-spectra\frequenzaufloesung.txt'],Δ_f,'\t');
159       disp('Finished.');
160      end
```

A.5 Appendix 5

Matlab routine for oscillating monopoles with parallel wave reflection at the end of the X coordinate. The coordinate system of the simulation is turned +90°. Therefore the X-axis is of the simulation is aligned with the Y-axis of the measurement.

```
1      % Calculating of oscillating monopoles
2      % circular expansion and overlap. #
3      % Monopoles shifte by relative coordinate system
4      % r^2 = x^2 + y^2 + z^2
5      % Lukas Wiesinger - 17.08.2017
6
7      clear all;
8      clc;
9      close all;
10
11     f=1000; %Hz
12     c=343; % m/s ; speed of sound
13
14     % setting field sice. best to use equal side ratios for cubes
15     x_size=1.65; % m
16     y_size=1.65; % m
17     z_size=0.22; % m
18
19     % plot size
20     x_plot=[0 900]; % mm
21     z_plot=[-0.11 0.11]*1000; % m
22     z_aspect=(max(z_plot)-min(z_plot));
23
24     % Coordinate system centered in Y and Z. runs from X 0:end, Y -y/2:+y/2, Z
25     % -z/2:+z/2
26
27     offset_x=[0 0]; %
28     offset_y=[0 0]; % describes the coordinates of each monopole from the center of the ...
           cube.
```

```
29      offset_z=[0.025 -0.025]; %
30
31      %% fine tuning for simulation
32      phase_shift=-0.3; %phase shift of signal
33      red_pot=0.75; % potence of reduction of wave. (Amplitude*1/r^_red_pot)
34      reflect_coef=0.1; % coefficent of reflection. How much gets reflected from 0 to 1;
35      Amp=0.7;  % Amplitude of wave
36
37      %% grid/video and therefore calc.-speed settings
38      n=300; %number of grid points. Not over 300. Big amount of memory will be needed.
39      time=1/f; % time in seconds;
40      Frames=0; % pictures made for movie in time; 0 = no movie, just plot, ignore error
41
42      %%
43      t_step=linspace(0,-time,Frames+1);
44
45      b=zeros(n,n,n);
46      B=zeros(n,n,n,length(t_step));
47
48      x=linspace(0,x_size*1000,n);
49      z=linspace(-z_size/2*1000,z_size/2*1000,n);
50
51      %% defitntion of variables with zeros for for loop
52      x_lin = zeros(1,n)';
53      y_lin = zeros(1,n);
54      z_lin = zeros(1,n);
55      X = zeros(n,n,n);
56      Y = zeros(n,n,n);
57      Z = zeros(n,n,n);
58      X_sq = zeros(n,n,n);
59      Y_sq = zeros(n,n,n);
60      Z_sq = zeros(n,n,n);
61      r_3d = zeros(n,n,n);
62      b = zeros(n,n,n);
63      B = zeros(n,n,n);
64      A = zeros(n,1,n);
65      z_lin=zeros(1,1,n);
66      figure('units','normalized','outerposition',[0 0 1 1])
67      for t=1:length(t_step)
68
69      if length(offset_x) ≠ length(offset_y) && length(offset_y)≠ length(offset_z)
70              error('redefine grid - coordinates missing')
71      end
72
73      %% Calculation of r^2 and from r^2 the amplitude, frequency ...
74      for of=1:length(offset_y)
75
76      x_lin=linspace(0,x_size,n)'-offset_x(of); %setting vectors with its length
77      y_lin=linspace(-y_size/2,y_size/2,n)-offset_y(of);
78      z_lin(1,1,:)=linspace(-z_size/2,z_size/2,n)-offset_z(of);
79
80      X=repmat(x_lin,1,length(y_lin),length(z_lin)); % creating a 3D array from the ...
            linear vectors
81      Y=repmat(y_lin,length(x_lin),1,length(z_lin));
82      Z=repmat(z_lin,length(x_lin),length(y_lin),1);
83
84      X_sq=X.^2; %squaring Matrices
85      Y_sq=Y.^2;
86      Z_sq=Z.^2;
87
88      r_3d=(X_sq+Y_sq+Z_sq).^0.5; %calculating the raidus for each matrix point
89
90      Amp_refl = Amp/repmat(r_3d(end,1:end,1:end),n,1,1).^red_pot; %Getting the last X ...
            slice of r for amplitude data
```

```
91      phase_refl = repmat(r_3d(end,1:end,1:end)./c * 2 * pi * f - phase_shift,n,1,1); ...
            %Getting the last X slice of r for phase data
92      d = Amp_refl.*sin(phase_refl + (flipud(X)./c + t_step(t))*f*2*pi); %calulating ...
            reflection
93
94
95      b=Amp./r_3d.^red_pot.*sin((r_3d./c+t_step(t))*f*2*pi-phase_shift); % calculating ...
            oscillating monopole
96      B(:,:,:)=B(:,:,:)+ b + reflect_coef*d; % calculating sound field for various ...
            reflections and monopoles
97      end
98
99      A=sum(B,2); % Summing in Y- Direction
100     A=squeeze(A);
101
102     hold on
103     subplot(2,1,1)
104
105     C=imagesc(x,z,flipud(rot90(A(:,:))));
106     set(gca,'YDir','normal','XDir','normal')
107     pbaspect([max(x_plot) z_aspect y_size ]) %weil in Y aufsummiert wurde d.h. XZ Plot
108     time_disp=sprintf('%f', abs(t_step(t)));
109     d=colorbar;
110     d.Label.String = 'Amp [a.u.]';
111     %text(.05,.1,[time_disp, ' sec'],'Units','normalized','FontSize',12);
112     xlabel('[mm] from the center')
113     ylabel('[mm] from the center')
114     xlim(x_plot)
115     ylim(z_plot)
116
117
118     title(['Soundwave at ' num2str(f),'Hz - 2 monopoles - 10% reflection @ X 1.65m'])
119
120     subplot(2,1,2)
121     plot(x,sum(A(:,:),2)) %summation in Z direction and Plot
122     title(['Integral value in Y and Z of the simulation @', num2str(f),'Hz']);
123     xlabel('[mm] from the center')
124     ylabel('Amplitude [a.u.]')
125     xlim(x_plot)
126     %ylim([-100000 100000])
127     pbaspect([max(x_plot) z_aspect y_size ])
128
129     F(t)=getframe(gcf);
130
131     %clf
132     end
133
134     % Writing video
135
136     video= VideoWriter('Monopoles','MPEG-4');
137     video.FrameRate=Frame_rate;
138     open(video)
139     writeVideo(video,F);
140     close(video)
```